Chapter 3

Receiver Function Analysis

3.1 Introduction

The receiver function method has been applied widely in the last 25 years by various research groups for estimating the partial impulse response of the crust and the upper mantle. The technique was originally developed by Langston (1979) and was then improved by various groups for different aspects such as spectral estimation, inversion etc. Some of the important developments on the technique are given in the studies of Ammon et al. (1990); Cassidy (1992); Owens et al. (1988); Park & Levin (2000); Sambridge (1999a); Shibutani et al. (1996).

Briefly, receiver functions rely on teleseismic earthquakes which sample the Earth along the travel path. By using the cancellation of the common features from the source and most of the path which are recorded on the different components, one can obtain the partial impulse response of the Earth just beneath the station. The estimated function is then used in an inversion schema for the calculation of a velocity-depth model in the vicinity of the station.

The recorded wavefield on the Earth can be described through a *convolutional model*. The source signal of the earthquake is convolved with many different operators from the origin time to arrival to the station. These operators represent near source effects, propagation path effects, near receiver effects and the instrument response. The isolation of the near receiver effects corresponds to the calculation of the receiver function.

It should be also noted that a typical receiver function trace will also carry signatures of local reverberations. Figure 3.1 depicts the propagation processes near a receiver. Incident teleseismic P waves can be converted to S waves at discontinuities that have a steeper path. P wave and S wave crustal reverberations contribute to the seismic signal at the receiver.

The details of the contributions to the convolutional representation are given below:

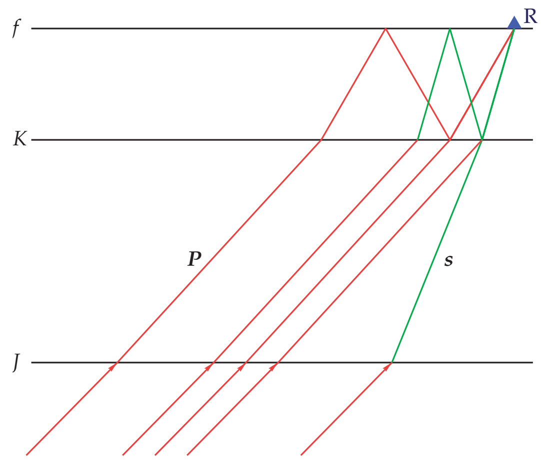

Figure 3.1: Propagation processes near a receiver (Kennett, 2002, p 320). f denotes the free surface. K and J are the seismic discontinuities.

Near Source Effects-N_S

Seismic waves emerging from a source will first interact with the local structure. The near source effects N_S include surface reflections (pP, pS, sP, sS), reverberations in the presence of a sedimentary layer and internal reflections due to the presence of strong reflector such as the Moho. All of these contributions shape the effective source time function for transmission to the teleseismic distance so that its nature becomes complicated.

Propagation Path Effects-P

In general sense, ray theory can be used to describe the passage of seismic energy inside the Earth. But to account for the correct energy of the seismic phase, some other contributions need to be taken into account.

The actual path of a ray will be affected due to lateral velocity variations as the dominant variations with depth. Focusing and defocusing occur for the traveling wave, which leads to multipathing. This can be seen as some of portion of the rays taking extra paths in addition to the main path (Stein & Wysession, 2003, p 188). The recorded waveform is the sum of the coherent parts of the rays which traveled on all possible paths from source to receiver. Multipathing is an important phenomena where strong velocity heterogeneties exist in the Earth, e.g., subduction zones and mid oceanic ridges.

For a propagating wave, the wavefront will grow along the propagation path. From the conservation of energy, the energy per wavefront decreases with distance from the source. Since the amplitude is proportional to the square root of energy, there will be a loss of amplitude for growing wavefronts. The whole process is called *geometric spreading*. There are two separate classes of geometric spreading for body waves and surface waves. The body waves passing through the volume of the material spread out more, and so decay quickly, than the surface waves whose energy is trapped near the surface.

The major discontinuities which define the transition zone between upper mantle and lower mantle are at 410 km and 660 km depth. Seismic velocities increase abruptly at these depths due to a change in the mineral structure. These rapid increases in velocity cause triplications in the arrivals. Upper mantle travel times show two triplications around 15° and 22° caused by the 410 and 660 km discontinuities (Stein & Wysession, 2003, p 171). For steeply incident waves, the amount of reflection from these zones will be small and most of the energy will be transmitted. Between 30° and 90° epicentral distances, the effect of structure is simplified, and this is the zone usually employed for receiver function analysis.

Although the Earth is assumed to be largely an elastic medium, there is a considerable amount of anelasticity. During the propagation of the rays, some seismic energy will be converted to thermal energy. The attenuation Q^{-1} defines this energy loss, and commonly there is a weak frequency dependency on the attenuation process. Generally speaking, an attenuation operator acts a low pass filter. Most studies of attenuation suggest a moderate loss factor in the crust ($Q_{\mu}^{-1} \sim 0.004$) slightly lower loss in the lithosphere with an increase in the asthenosphere of the upper mantle ($Q_{\mu}^{-1} \sim 0.01$) and then a decrease to crustal values, or lower, in the mantle below 1000 km (Kennett, 2001, p 147).

***Near Receiver Effects-*N_R**

As for the near source effects, the heterogeneous structure in the neighbourhood of the receiver dominates the seismic wave. A sedimentary layer on top of the basement will lead to reverberations.There is also an amplification due to free surface effects on the recorded displacements. The interaction of P

and S waves at the Earth's surface leads to differential amplification between the vertical and horizontal components. Reading et al. (2003b) demonstrated a method to remove this amplification effect from RF traces. The benefit is that the subsequent inversion procedure spends less time fitting the high amplitude of direct P arrivals and most time fitting the later parts of the RF that provide information on the crust and uppermost mantle structure.

Combination of Effects

If we want to make a physical realization of these various processes, the three classes of propagation effects act on the source time function as a set of cascade connected linear systems. In addition to these effects, the instrument response $I(t)$ needs to be added to the model. The final output of the last system creates the displacement of the Earth at the receiver $u(t)$. The cascade representation corresponds to a convolutional model, a linear system has superposition properties and thus can be implemented as the operation of convolution. Although our system in general is linear, some effects like reverberations operate recursively.

If we represent the combination of effects mathematically, then the three orthogonal components of the displacement, u_V on the vertical, u_R the radial component on the great circle between source and receiver and u_T the tangential component in the horizontal plane can be represented as

$$\begin{aligned} u_V(t) &= s(t) * N_S * P(t) * N_{R_V} * I(t) \\ u_R(t) &= s(t) * N_S * P(t) * N_{R_R} * I(t) \\ u_T(t) &= s(t) * N_S * P(t) * N_{R_T} * I(t) \end{aligned} \tag{3.1}$$

where $*$ denotes the convolution operator and t is time variable.

This relation is represented in the time domain. However, the multiplicative representation in the frequency domain of the convolution operation will be easier for the isolation of the near receiver effects. Then we can rewrite the eq.(3.1) in frequency domain as

$$\begin{aligned} u_V(\omega) &= s(\omega) \cdot N_S \cdot P(\omega) \cdot N_{R_V} \cdot I(\omega) \\ u_R(\omega) &= s(\omega) \cdot N_S \cdot P(\omega) \cdot N_{R_R} \cdot I(\omega) \\ u_T(\omega) &= s(\omega) \cdot N_S \cdot P(\omega) \cdot N_{R_T} \cdot I(\omega). \end{aligned} \tag{3.2}$$

The terms common to the three components can be eliminated by deconvolution, e.g., by taking the spectral ratios of the radial component with another. For the coda of P waves, it is normal to deconvolve the radial component with the vertical component to emphasize the converted S waves on the radial component. This operation is expected to lead to the emergence of N_{R_R} term from other contributions.

To extract N_{R_R} and N_{R_T} from the ground displacement, various deconvolution methods can be applied. The motivation behind trying different methods is to find the procedure that results in the optimum structural response. At present, the deconvolution method in most common use is the spectral division method which also corresponds to *Wiener Inverse Filter*. Other deconvolution methods, homomorphic deconvolution, multitaper estimation and a wavevector approach, may be preferable in some cases. In the following section, alternative methods are outlined and data examples from the TASMAL project are presented. An appraisal of the different methods is then given.

3.2 Method Development

A range of different approaches for deconvolution have been investigated. In each case I have written my own code (Fortran and Matlab routines) to implement the algorithms.

Spectral Division

Deconvolution via spectral division is the generalized version of an optimum inverse filter (also called as Wiener Inverse Filter (Proakis & Manolakis, 1988)).

If we know the input and the output for a unknown system, we can estimate the transfer function of the unknown system by using an iterative least squares method.

Let $x(t)$ represent as the input, $y(t)$ the actual output, $d(t)$ the desired output and introduce $e(t)$ as the difference between the desired and the actual output. This schema tries to match the FIR (finite impulse response) based system to an unknown system function by minimizing the difference between desired output and actual output. If we denote the coefficients of the FIR based model as b_k; r_{xx} as autocorrelation of input; and r_{dx} as cross-correlation of desired output $d(t)$ and input $x(t)$ then the final form of the filter will be as in eq.(3.3). This relation is known as the *Wiener-Hopf equation*.

$$r_{dx}(l) = \sum_{k=0}^{M} b_k r_{xx}(k-l), \quad l = 0, 1, ..., M. \tag{3.3}$$

If we take Fourier Transformation of both sides of eq.(3.3) then the relation will be

$$H(\omega) = \frac{\psi_{dx}(\omega)}{\psi_{xx}(\omega)}. \tag{3.4}$$

In eq.(3.4), $H(\omega)$ is the transfer function of the unknown linear system, $\psi_{dx}(\omega)$ is the cross-spectral density of $x(t)$, $d(t)$ and $\psi_{xx}(\omega)$ is the density spectrum of $x(t)$ which is also equivalent to $|X(\omega)|^2$.

After transforming to the frequency domain, N_{R_R}/N_{R_V} and N_{R_T}/N_{R_V} can be found by a spectral division of $u_R(\omega)$ and $u_T(\omega)$ by $u_V(\omega)$.

Because of the finite frequency band, $u_V(t)$ can be thought of as band-passed delta function in time $\delta(t)$, then

$$N_{R_R} = \frac{u_R(\omega)u_V^*(\omega)}{u_V(\omega)u_V^*(\omega)} \tag{3.5}$$

$$N_{R_T} = \frac{u_T(\omega)u_V^*(\omega)}{u_V(\omega)u_V^*(\omega)}, \tag{3.6}$$

where $*$ denotes the complex conjugation, the relations in eq.(3.5) and (3.6) are obtained by using the relation in eq.(3.4).

In practice, the denominator of eq.(3.4) can have spectral gaps which can be viewed as numerical values of the spectrum $|X(\omega)|^2$ close to 0. The spectral division in this case will lead to numerical unstability. To avoid numerically unstable operations, spectral division can be performed in two different ways. In the first case, the holes of the denominator are filled with a predetermined constant value ($c.\max[u_V(\omega)u_V^*(\omega)]$). This operation is called *Water-Level Deconvolution*. Alternatively biasing the denominator with a constant value ($c.\max[u_V(\omega)u_V^*(\omega)]$) provides numerical stability at the expense of a slight systematic error in the estimate of the transfer function.

Eq.(3.5) can be rewritten with *Water-Level Deconvolution* applied as

$$N_{R_R} = \frac{u_R(\omega)u_V^*(\omega)}{\phi_{ss}(\omega)}, \tag{3.7}$$

where

$$\phi_{ss}(\omega) = \max\left[u_V(\omega).u_V^*(\omega), c.\max[u_V(\omega)u_V^*(\omega)]\right]. \tag{3.8}$$

In general, the choice for the *water-level* or *biasing* parameter is found by trial and error, since the quality of the receiver function signal is dependent on the individual records. The aforementioned section covers the theoretical basis for the P to S converted receiver function generation. However, by interchanging the order of components on the deconvolution, one can estimate the S to P converted phases. This approach has been successfully applied on crustal and mantle scale by Farra & Vinnik (2000).

Although the plain spectral division of the displacements with the *water-level* correction is the most common technique for calculating the receiver functions, a number of different approaches have also been investigated to try to improve the estimation of the RF.

In figure 3.2, the effect of the water-level and biasing parameters are shown for the stacked radial receiver functions of station TL06 from 40 individual estimates. The raw spectral division could not recover the any of the conversion of the P to S in the radial receiver function. With the increasing biasing parameter, the deterministic signals appear around 5 sec, 10 sec and after 15 sec. Besides the increase in the amplitude of the receiver functions, biasing leads to consistent results on the waveform shapes. In the water-level deconvolution, the increasing values of the water level results in an averaging operation on the waveform shapes which causes loss of resolution in the wavetrain. This effect is most visible on the later arrivals (after 15 sec). Resolution loss on the waveforms can be an important issue on the inversion step of the observed receiver functions where the inversion also relies on the shape of the waveforms.

Homomorphic Deconvolution

Homomorphic deconvolution was originally developed as a method for eliminating the echoes on voice records by Oppenheim (1969). In this method, the output signal $y(t)$ is again assumed to be the convolution of the input $x(t)$ and some system function. The difference is that this method works in cepstral domain D. If the convolution form of input and system function, which is the structural response in our case, is transformed to an addition

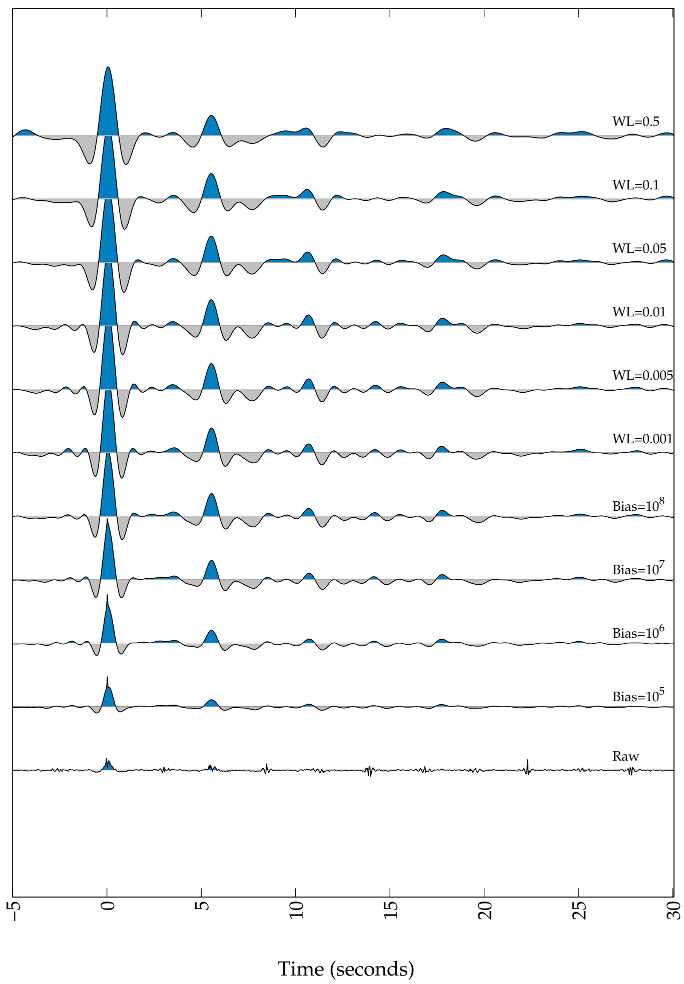

Figure 3.2: The effect of water-level and biasing parameters on the stacked radial receiver function estimates from station TL06. For biasing the results are consistent with the increasing values but amplitudes grow. In water-level deconvolution, increase in water-level parameter results resolution loss on the estimates.

operation then a filter L can be applied to extract the system function from output. For achieving this, the following operations are applied to the input signal $x(t)$. Firstly, Fourier Transformation of the signal is made. Secondly, the logarithm function will be applied to the sequence which is in the frequency domain. Finally, the inverse Fourier Transformation is applied to the signal. The final form is called as *the cepstrum*. The relation of the cepstrum $\widehat{x}(t)$ and the original signal $x(t)$ is shown in eq.(3.9).

$$\widehat{x}(t) = \frac{1}{2\pi}\int_{-\infty}^{\infty} \log\left[\int_{-\infty}^{\infty} x(t)\mathrm{e}^{-\mathrm{i}\omega t}dt\right]\mathrm{e}^{\mathrm{i}\omega t}d\omega \tag{3.9}$$

Since we know that our output $y(t)$ is the convolution of input $x(t)$ and some system function $s(t)$, this relation (eq. (3.9)) will correspond to addition in the cepstral domain. If a suitable filter L is applied then system function can be extracted from the output $y(t)$.

The convolutional property is translated to additivity in *the cepstral domain* via taking the logarithm of the signal. The term of *cepstral domain* is the spectrum of the log of the spectrum of a time waveform (Oppenheim & Schafer, 2004). By finding the right filter, one can eliminate the unwanted contributions and isolate near-receiver effects. However, in practice, this approach may be problematic for the receiver function case. The main assumption is that the input signal is *minimum phase*. For earthquake sources, this assumption is not always satisfied. Homomorphic deconvolution is quite sensitive to the presence of noise. This processing schema was applied by Crosson & Dewberry (1994) and Li & Nábělek (1999) to receiver functions. Bostock (2004) proposed a shaping filter to be applied to seismic signals to satisfy the *minimum phase* criteria.

In figure 3.3, the comparison between receiver functions from water-level and homomorphic deconvolution is made. Although the results from the homomorphic deconvolution is promising, the filtering process in the log spectral domain needs extensive testing for better results.

Multitaper Estimation

Since the spectral division belongs to the class of spectral estimation problems, the use of appropriate data windows or tapering is essential. With the right choice of window, one can improve the variance, resolution and leakage characteristics of the final estimate. Briefly, these terms refer to the variability of the estimation for each of the realization of the signal, resolving the right frequency bins and the amount of unwanted contributions from the different part of the signal.

Slepian tapers are a class of orthogonal windows which ensure that the maximum spectral concentration is achieved on a band limited signal. The

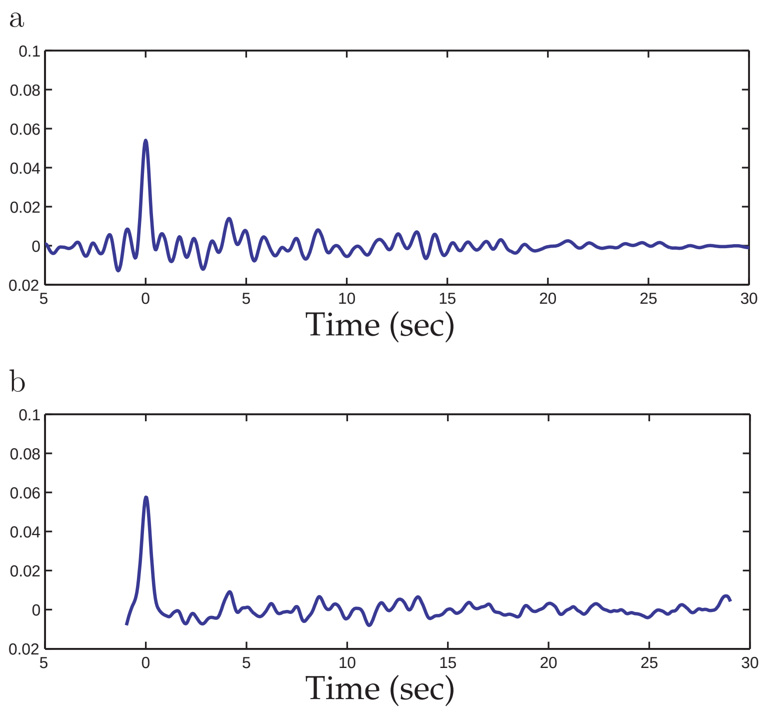

Figure 3.3: The comparison between two different receiver function estimation techniques. a) Plain spectral division with water-level correction. b) Homomorphic deconvolution via filtering in log spectral domain. In both of the receiver functions, the Moho conversion before 5 sec is recovered but Homomorphic deconvolution is much more sensitive to the choices made with respect to bandwidth, and other parameters and so is more difficult to implement as a routine technique.

estimation of the shape of these windows is an eigenvector problem and the corresponding eigenfunction forms the data window.

If we denote $x(t)$ as a time limited signal with length T, and $X(f)$ as bandlimited function with bandwidth W, then the concentration in time domain $\alpha^2(t)$ can be shown to be expressed as

$$\alpha^2(t) = \int_{-T/2}^{T/2} |x(t)|^2 dt \bigg/ \int_{-\infty}^{\infty} |x(t)|^2 dt \ . \tag{3.10}$$

Also the concentration problem can be also expressed in the frequency domain as an integral equation (eq.(3.11))

$$\int_{-W}^{W} K(f, f^{'}; T) X_w(f^{'}) df^{'} = \alpha(t)^2 X_w(f) \quad |f| \leq W, \tag{3.11}$$

where

$$K(f,f^{'};T)=\frac{\sin\left[\pi T(f-f^{'})\right]}{\pi(f-f^{'})}. \tag{3.12}$$

The problem is now finding such kernels (windows) $K(f,f^{'};T)$ that maximize the concentration $\alpha^2(t)$. The solution of this integral equation is an eigenvector problem. The kth eigenfunction of the kernel ψ with its associated largest kth eigenvalue λ will form the solution. After making the substitutions ($x \equiv f/W, \quad y \equiv f^{'}/W, \quad c \equiv \pi WT$), the integral equation becomes

$$\int_{-1}^{1}\frac{\sin\left[c(x-y)\right]}{\pi(x-y)}\psi(y;c)dy=\lambda(c)\psi(x;c), \quad |x|\leq 1. \tag{3.13}$$

The solution set of the eigenfunctions are called *discrete prolate spheroidal sequences* or *Slepian sequences*. This set was introduced by Slepian (1978). Each of the possible tapers corresponds to a maximum eigenvalue.

The multitaper method uses an multiple window approach to construct a good balance between the variance and the bias properties of the spectrum by using Slepian Sequences. Eigenspectrums are calculated via tapering with different spheroidal sequences. The kth eigenspectrum is shown in eq.(3.14) where the $h_{t,k}$ is kth data taper for input x_t

$$\widehat{S}_k^{mt}(f)=\Delta t\left|\sum_{t=1}^{N}h_{t,k}x_t\mathrm{e}^{-\mathrm{i}2\pi f t\Delta t}\right|^2. \tag{3.14}$$

Afterwards, the eigenspectrums are averaged to form a spectral estimate with low variance. The determination of the appropriate order of the tapers plays a major role in the characteristics of the final spectrum. For low orders, the bias will be small and the variance level will be low for higher orders. The final spectra is given by eq.(3.15)

$$\widehat{S}^{mt}(f)=\frac{1}{K}\sum_{k=0}^{K-1}S_k^{mt}(f). \tag{3.15}$$

The details of the algorithm are presented in Thomson (1982) and Percival & Walden (1993).

The time-bandwidth product determines frequency resolution of the estimates. Spectral variation over small intervals in the frequency domain corresponds with widely spaced features in the time domain (Park & Levin, 2000). On the other hand larger K values lead to lower variance in the cost of spectral leakage.

In figure 3.4, the estimates of radial receiver functions from the multitaper method with Slepian tapers are shown with a set of different time-bandwidth product values (NW) and different number of Slepian tapers (K). For comparison an estimate from the plain water-level deconvolution (wl) was included. At first glance, the difference in the estimates for lower and higher time-bandwidth product is obvious, e.g., K=2, NW=2.0 and K=2, NW=3.5. The larger time-bandwidth product (NW=3.5) resolved the later arrivals appeared after 20 sec due to the property that spectrum estimates with higher values of time-bandwidth product will have more resolution. The multitaper estimates have some fundamental differences between the estimate from the wl on the waveform shape. Although the amplitudes of wl estimate is higher than the multitaper, the general signal to noise ratio is lower. This result has a significance on the inversion step where the nonlinear solver tries to fit full waveform for finding a solution. In addition to this, the signals between the deterministic arrival due to the noise have been suppressed in the multitaper estimates.

The multitaper approach with the Slepian tapers was applied to receiver functions by Park & Levin (2000) with a demonstrated improvement in the results compared to simpler methods. However, the implementation of the Slepian tapers is not straightforward. An equivalent and better class of windows was developed for estimating plasma fluctuations by Riedel & Sidorenko (1995). These tapers use the sine functions, therefore they are easier to implement and can be also used in the multitaper context. Also recently Helffrich (2006) proposed an extended schema for multitaper methods applied to receiver functions.

Wavevector Approach

The observed displacement field on the surface is a result of interaction of the wavefield and the free surface as shown below. If the *Snell's Law* is defined for incoming plane P and S waves, then

$$p = \frac{\sin i}{\alpha_0} = \frac{\sin j}{\beta_0}, \tag{3.16}$$

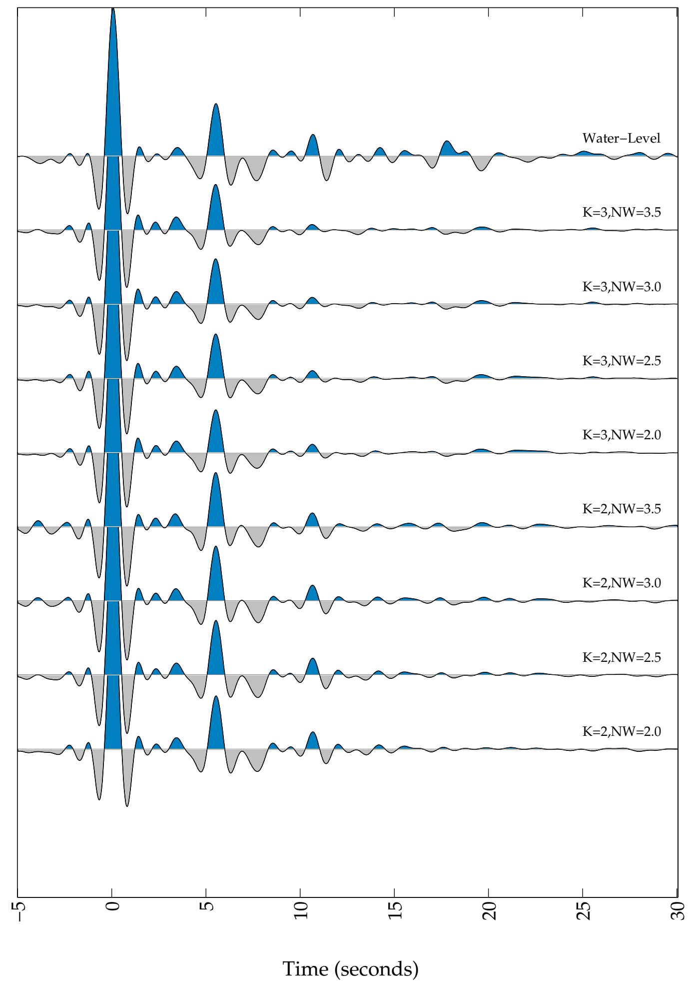

Figure 3.4: Radial receiver functions from multitaper method for a set of different time-bandwidth product values (NW) and different number of Slepian tapers (K) compared with plain water-level deconvolution of 0.01. Each of the traces has been normalized to unity to emphasize the changes in the signal.

where i, j and α_0, β_0 are the angle of incidence and velocity for P and S waves and p is the corresponding ray parameter.

In the case of an impinging P wave with an amplitude of A, the displacement field in the corresponding components Z_u, vertical and R_u, horizontal will be

$$Z_u = A\cos i, \qquad R_u = A\sin i, \tag{3.17}$$

where i is the angle of incidence. This relation does not include any free surface effect. The influence of free surface reflection can be introduced by inserting amplification operators $C_{1,2}$ in eq.(3.17) so that the eq.(3.17) with the amplification becomes

$$Z = A\cos i \cdot C_1, \qquad R = A\sin i \cdot C_2. \tag{3.18}$$

After the free surface interaction, the effective incidence angle changes, this is called as the *apparent angle* of incidence i_f. This can be seen from the ratio of the Z and R components as

$$\tan i_F = \frac{R}{Z} = \frac{R_u \cdot C_2}{Z_u \cdot C_1} = F\tan i, \tag{3.19}$$

where surface amplification factor F is

$$F = \frac{C_2}{C_1} = \frac{2\cos i\cos j}{1 - 2\beta_0^2\sin^2 i/\alpha_0^2} = \frac{2\cos i\cos j}{1 - 2\sin^2 j}. \tag{3.20}$$

The free surface effect can be generalized for all three rotated components Z, R and T in the direction of source-receiver azimuth. By following the convention of Kennett (1991), we can write the isolated P, S_V and S_H wavefields from the displacement which was recorded on the components as

$$\begin{pmatrix} P \\ S_V \\ S_H \end{pmatrix} = \begin{pmatrix} -V_{PZ} & V_{PR} & 0 \\ -V_{SZ} & V_{SR} & 0 \\ 0 & 0 & V_{HT} \end{pmatrix} \begin{pmatrix} Z \\ R \\ T \end{pmatrix}$$

where free surface correlation coefficients are

$$V_{PZ} = -(1 - 2\beta_0^2 p^2)/(2\alpha_0 q_{\alpha_0}) \tag{3.21}$$

$$V_{SR} = (1 - 2\beta_0^2 p^2)/(2\beta_0 q_{\beta_0}) \tag{3.22}$$

$$V_{PR} = p\beta_0^2/\alpha_0 \tag{3.23}$$

$$V_{SZ} = p\beta_0 \tag{3.24}$$

$$V_{HT} = 0.5 \tag{3.25}$$

and vertical slownesses are

$$q_{\alpha_0} = \sqrt{\alpha_0^{-2} - p^2}, \quad q_{\beta_0} = \sqrt{\beta_0^{-2} - p^2}. \tag{3.26}$$

This correction is carried and by empirically chosen appropriate velocities.

Wavevector form of the receiver function has been used by Reading et al. (2003b) for improving the inversion methodology. Also Bostock (1998) used the transformation for the suppression of multiples and the wavefield decomposition.

Unlike the coordinate rotation with a chosen angle such as LQT transformation (Vinnik, 1977), this method assigns the correct energy on the components by transformation with the velocity information. This is illustrated in an example using data from station TL06. The wavevector form of the radial receiver functions were computed with a P wave velocity of 5.8 km/sec and S wave velocity of 3.4 km/sec. The ray parameter was computed via ray tracing with the model AK135 (Kennett et al., 1995) for the corresponding epicentral distance of the earthquake. In figure 3.5, the S-wavevector receiver functions are shown with the conventional radial receiver functions. In the wavevector form, the main peak due to the P arrival is suppressed; however, the P to S wave conversion at 5 sec is preserved including the later arrivals. With the wavevector form of the receiver functions, the inversion of the waveforms will concentrate more on the region of interest (Moho conversion arrival and later arrivals) than the conventional form of the radial receiver functions, where the main P phase has a dominant signature on the estimated signal.

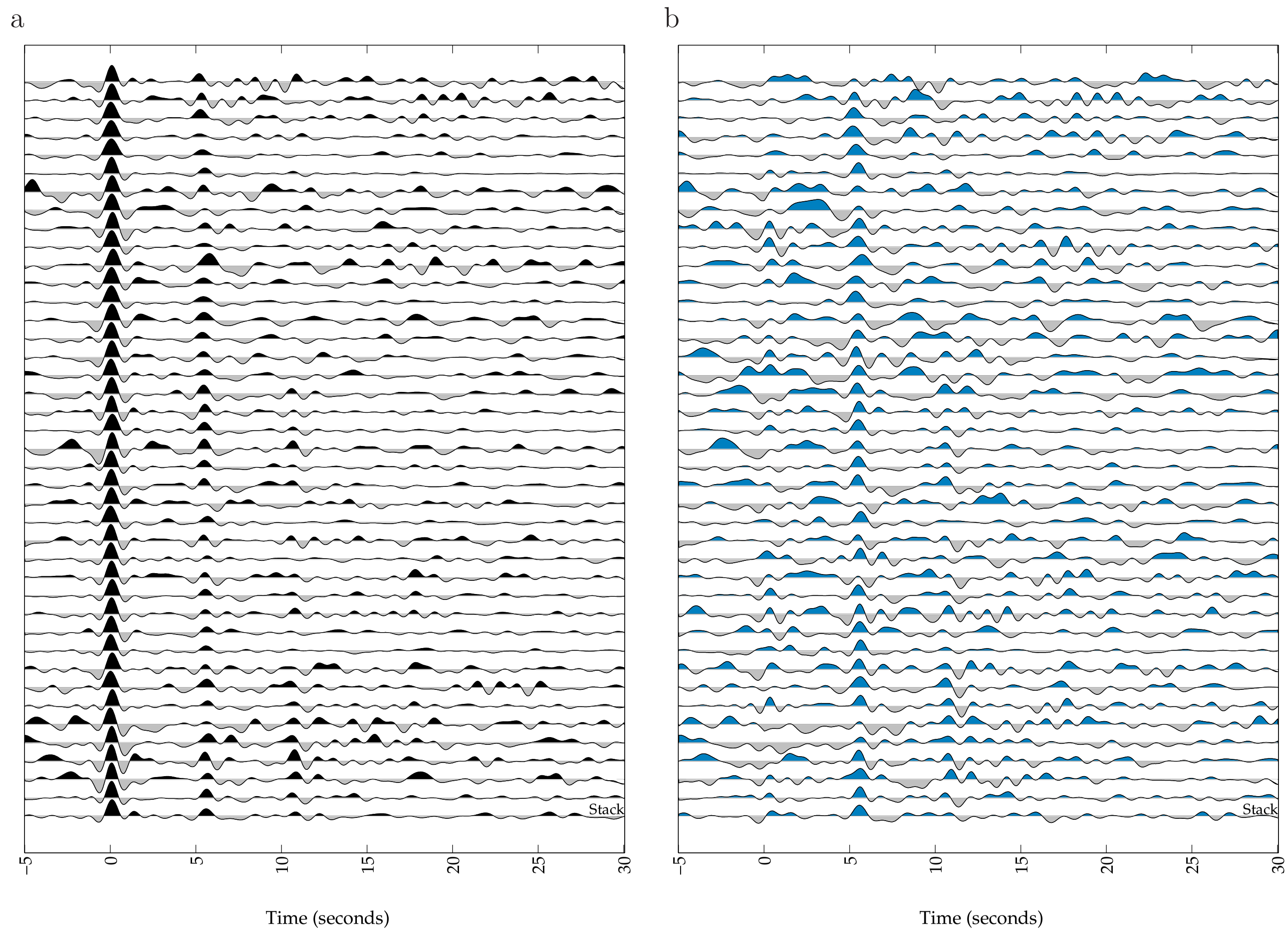

Figure 3.5: a) Radial receiver functions (black) from TL06. b) S-wavevector form of the radial receiver functions (blue) from TL06. For both of the panels, the bottom trace was produced from stacking all of the shown receiver functions.

3.2.1 Appraisal of Different Methods

The methods given in the previous sections can be compared together with their advantages and weaknesses in particular situations.

Plain spectral division with 'water-level' correction is the simplest and least rigorous method of the computation of receiver functions. Despite its simplicity, it has some major drawbacks. Unless proper windowing is applied in frequency domain, the control on the variance, leakage and bias will be minimum. These parameters can be quite important, if the signal to noise is low. The closely related technique 'biasing' can produce better estimates with the right parameter choice. In frequency domain, the biasing will be equivalent to the pre-whitening of the spectrum. In some cases, this is required to broaden the spectrum. Although the application is quite different from the generation of receiver functions, this method was successfully applied on broadening the spectrum of ambient noise wavefield in a later part of this study.

Homomorphic deconvolution is a powerful deconvolution technique, first applied on eliminating the echoes on the voice records by Oppenheim (1969). However, the properties of homomorphic systems make it difficult to fulfill with teleseismic signals. The minimum phase condition is often not satisfied by the seismic records. Bostock (2004) assumed the incoming P wave has minimum phase character and then applied a shaping filter to normalize the P wave and therefore emphasize the direct arrivals. As a result, multichannel type of deconvolution on the source normalized P wave signals in log spectral domain gave better Green's function estimates. Another way to exploit the homomorphic filtering in the context of receiver function, is to apply a filter in log spectral domain to suppress the unwanted part. However, to apply this successfully, a precise knowledge of the spectrum is needed, which is commonly not known.

Multitaper estimation is one of the most significant techniques applied to spectral estimation problems. The windowing of the data before the spectral estimation is a common practice to suppress some of the unwanted effects on the final estimates, e.g., reducing spectral leakage, controlling variance etc. In multitaper estimator case, multiple parameters can be controlled at the same time to have better result. The power of multitaper technique comes from the specialized windows applied on the signal, which offer maximum spectral concentration for bandlimited signal, e.g., seismic signals. Then with the right type of averaging, the variance characteristics of the estimates can be controlled. The plain spectral division with water-level or biasing correction can not offer these controls on the estimates. It can be concluded that the multitaper technique is a corrected form of the plain spectral division. There are two difficulties associated with multitaper estimation. In the classical form, the chosen windows are Discrete Prolate Slepian tapers, which can be computationally intensive to calculate. However, sinusoidal type of tapers with similar properties of Slepian tapers were introduced by Riedel & Sidorenko (1995) with less computational complexity. The second potential difficulty with the multitaper estimation for the receiver function generation is about the choice of design parameters. The increased frequency resolution can result in widely spaced features in time domain, therefore loss of resolution in this domain (Park & Levin, 2000). As a result, the time-bandwidth product (NW) has to be tested extensively before processing bigger datasets.

The last technique which can improve the estimates, is the wavevector approach applied by Reading et al. (2003b) to receiver functions for eliminating the free surface response. Unlike the aforementioned techniques, this method does not rely on the signal processing schemes. This approach gains considerable importance on the type of inversion where the full waveform is modelled. The removed free surface response on the records emphasizes the later arrivals. The major difficulty of this technique is the requirement of good velocity knowledge of P and S waves to successfully remove the free response. This priori information may not be available in all cases. The wavevector method works best when the surface velocities are quite high. It can be adapted to suppress near surface sediment multiples, but this requires very detailed knowledge of the near surface conditions and is rather tricky to use.

In this work, multitaper estimator was used with the following parameters of time-bandwidth product: NW=2.5 and taper order: K=3 in the receiver function generation both for the observed and synthetic data. The computer programs used in the generation of the examples given for each technique and for the receiver functions of the whole TASMAL experiment were written as a part of this work. The wavevector approach has been used to check the identification of the Moho arrival, but not directly in the inversion.

3.3 Geophysical Inversion

Before going into the details of the geophysical inversion used for the extraction of near-receiver velocity information from receiver function, we need to address some general issues such as the definitions of *the forward and inverse problems*. The forward problem can be defined as calculating the data from a given physical model. This can be visualized as calculating the position vector h of a free-falling object for some time interval t by using the basic relation of $h = 1/2gt^2$ where the resistance of the air is neglected and g is the acceleration of gravity. This is a simple example of a *forward problem*. On the other hand if we had only measured the position vector values h of this free-fall motion, how can we estimate the time values t which corresponds to our observed values of position h, with a chosen model. This estimation problem and its solution set's appraisal correspond to *the inverse problem*.

The forward problem can be defined in 2 different ways. First, it can be represented as nonlinear problem as in eq. (3.27), where d is the calculated data, $G(\mathbf{m})$ is the functional operator, and $\mathbf{m}$ is the model parameters

$$d = G(\mathbf{m}). \tag{3.27}$$

The second approach is to think of the problem directly in a linear sense in which case it can be written as in eq. (3.28) with discrete parameterization. If the data corresponding to a reference model $\mathbf{m}_0$ is d_0, then local linearisation gives

$$d_i - d_0 \simeq G_{ij}(\mathbf{m}_j - \mathbf{m}_i)$$

with

$$G(\mathbf{m}) = \partial d_i / \partial \mathbf{m}_j,$$

where

$$d_i = \sum_j G_{ij}\mathbf{m}_j. \tag{3.28}$$

In all cases, a misfit criteria should be defined for fitting the data to the model. Commonly minimization of the difference between the observed and calculated data is chosen and shown in eq. (3.29) in least squares sense,

$$\phi(d, \mathbf{m}) = (d_{obs} - G\mathbf{m})^T (d_{obs} - G\mathbf{m}), \tag{3.29}$$

where the d_{obs} is the observed data and Gm product represents the calculated data. If we write the linear forward problem in matrix form,

$$G\mathbf{m} = d$$

then, a solution can be obtained using the least squares solution

$$\mathbf{m}_{est} = (G^T G)^{-1} G^T d. \tag{3.30}$$

In the nonlinear case, the problem can not be directly stated as $d = G\mathbf{m}$. The solution strategies will vary according to the scale of the nonlinearity. It can be linearized and solved as above, or by using some advanced algorithms such as direct search procedures.

Most geophysical problems exhibit nonlinearity. With increasing computational power, it is desirable to solve nonlinear inverse problems with better estimation techniques. The linear geophysical inverse theory is widely given in Menke (1984), Tarantola (1987), Parker (1994), and Snieder & Trampert (1999).

Neigbourhood Algorithm

The stacked receiver function data has to be mapped from time section to depth in order to model the velocity structure underneath a station. Generalized inversion plays a major role on this transformation. However, there is a strong nonlinear dependency of the receiver function signal on the shear wave velocity. This dependency has a profound effect on the inversion schema to be carried out. Ammon et al. (1990) showed the effects of the linearization and the nonuniqueness of the receiver function inversion. Shibutani et al. (1996) applied a nonlinear genetic algorithm type of inversion to data from an earlier Australian deployment and was able to recover the velocity structure for the crust. An improved algorithm was proposed by Sambridge (1999a,b) with a fully nonlinear, derivative free direct search algorithm (Neighbourhood Algorithm; hereafter called NA) assisted by the geometrical constructs of Voronoi cells. This approach is conceptually simpler than any linearized schemes (these methods are dependant on the calculation of the partial derivatives). NA is used for inverting the observed receiver function in this study.

The evolution of the Voronoi cells in an NA inversion example is given in figure 3.6 for different numbers of points in 2-D space.

The summary steps which are taken by the NA are as follows.

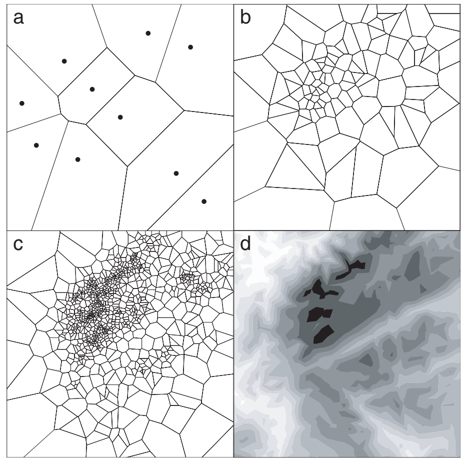

Figure 3.6: Regions of Voronoi cells for different sampling points. a) 10. b) 100. c) 1000. d) Contours of the test objective function (Sambridge, 1999a).

1. Generation of model samples n_s uniformly in parameter space with associated Voronoi cells.

2. Calculation of the misfit functions from the generated models and rank the lowest misfit models n_r.

3. Creation of new models n_s inside the Voronoi cells of lowest misfit models n_r by uniform random walk.

4. Reiterate from step 2.

The style of the crustal model for Australia which is used in the inversion stage has been inherited from the work of Shibutani et al. (1996). The general layout of the model is a sediment layer on the top, basement layer, upper crust, middle crust, lower crust and uppermost mantle. Each layer consists of S wave velocities V_s for the upper and lower parts, thickness h and V_p/V_s ratio. As a result, 24 parameters are calculated during the inversion of the data.

Another important feature of the NA algorithm is that it creates an ensemble of models rather than a single best model. This creates the opportunity to assess the set of searched and compare well-fitting models.

3.4 Data

In the recent past, numerous broadband seismic experiments have taken place across the Australian continent. The TASMAL experiment ran between 2003 to 2005 with 20 stations with the aim of revealing the structural boundary of Precambrian and Phanerozoic blocks in central and eastern Australia. To characterize the Gawler Craton and its surroundings in south Australia, 4 additional broadband stations were deployed in the similar time frame of TASMAL but ran for a shorter time than the TASMAL experiment. The collected data from these deployments were used with the receiver function method to characterize the Moho depth and its nature.

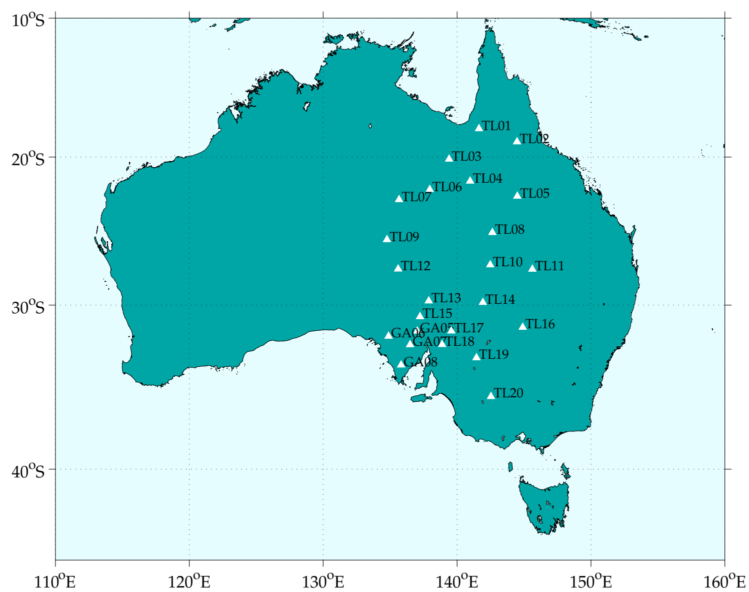

Figure 3.7: The location of three component broadband stations of the TASMAL experiment (TL) and its Gawler Craton extension (GA) shown with white triangles.

Seismic data from epicentral distances of between 30° and 90° were used to avoid triplication in the mantle (as discussed in an earlier section) and to ensure that the arriving seismic waves will be steeply incident and hence, the conversion ratio of the seismic phase will be high enough. The magnitude interval for events was chosen between 5.5 and 6.5 which is sufficient for a high signal to noise ratio and avoids the complicated and elongated waveforms of higher magnitude events.

For mapping the energy to the components, the horizontal components were rotated geometrically to radial and transverse parts by using the connecting azimuth plane of the source and the receiver. Each of the arrivals was picked by using the theoretical arrival time generated by the model AK135 (Kennett et al., 1995) with a time window of 60 seconds. Multitaper spectral estimation with Slepian tapers was used on the observed receiver function generation. The *water-level* for the deconvolution which is shown at eq.(3.8) was set as 0.01 after several tests. By visual inspection, the generated receiver functions were classified according to the waveform shape. It should be stated that the receiver function generation is quite sensitive to the noise levels and other artifacts on the data. Roughly, for each of the stations 10% of the records proved satisfactory due to aforementioned limitations. The receiver function waveforms are classified according to their backazimuths. In table 3.1, the details of the generated receiver functions for each of the station are given. Due to the nonuniform coverage of seismicity around the Australian continent, some of the backazimuthal ranges offer higher number of events suitable for receiver function analysis, e.g., $270° - 360°$ therefore used frequently.

Also by comparing the radial receiver functions of the other available backazimuthal ranges, the geometry of the structure was assessed. Although the planar structure of the layering is the main assumption, numerical studies show that in the presence of dipping layers or anisotropy, energy will be variable on the radial and transverse receiver functions which belong to different backazimuths (Cassidy, 1992). These type stations were marked with '3-D'. However for some of the stations, e.g., TL01, TL11, under the strong influence of sedimentary structures, different backazimuthal ranges have similar record sections. In reality, this may not reflect the presence of 1-D crustal structure, since Moho conversion is masked in these receiver functions. In figure 3.8, for two different stations; TL04 and TL11, the radial receiver functions are presented which belong to two different backazimuthal ranges. In figure 3.8a, the Moho transition is clear at 5 sec. However, figure 3.8b shows the clear effect of the surface sediments on the receiver functions, where Moho conversion is masked with reverberations.

Station	Good RF Events	Structure	Backazimuth Range
TL01	96	1-D	$190° - 360°$
TL02	85	1-D	$270° - 360°$
TL03	68	3-D	$270° - 360°$
TL04	40	1-D	$0° - 30°$
TL05	50	1-D	$270° - 360°$
TL06	60	1-D	$80° - 120°$
TL07	29	3-D	$270° - 360°$
TL08	86	3-D	$270° - 360°$
TL09	22	1-D	$80° - 120°$
TL10	46	1-D	$270° - 360°$
TL11	57	1-D	$270° - 360°$
TL12	110	3-D	$270° - 360°$
TL13	102	1-D	$270° - 360°$
TL14	268	1-D	$270° - 360°$
TL15	35	3-D	$270° - 360°$
TL16	139	1-D	$270° - 360°$
TL17	131	1-D	$270° - 360°$
TL18	31	3-D	$20° - 100°$
TL19	105	3-D	$270° - 360°$
TL20	48	1-D	$270° - 360°$
GA05	18	3-D	$270° - 360°$
GA06	20	1-D	$270° - 360°$
GA07	12	1-D	$270° - 360°$
GA08	7	3-D	$270° - 360°$

Table 3.1: The details of the radial receiver functions used in this study. The number of receiver functions, estimated structure geometry and backazimuth range used in the final stack are given.

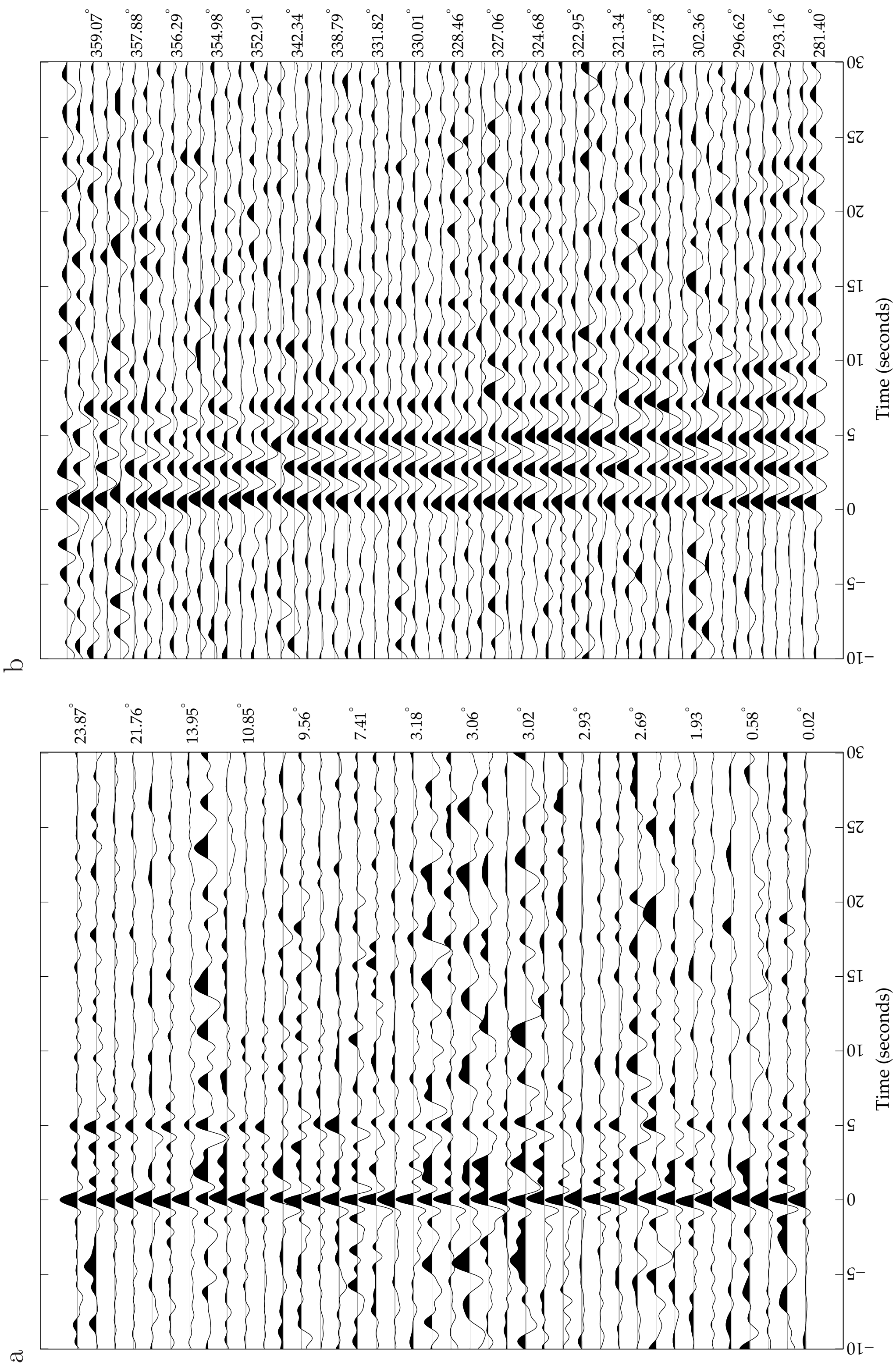

Figure 3.8: Radial receiver functions for a) TL04 with backazimuths between 0° − 30°, and b) TL11 with backazimuths between 270° − 360°. TL04 contains the clear Moho conversion at 5 sec. TL11 shows the influence of the thick surface sedimentary layer on the receiver functions.

3.5 Results of Inversion

The observed radial receiver functions were inverted with the NA for various different parameter ranges to exploit the dependence of the inversion results to the starting choice of the model parameters. Results were then merged and weighted inversely according to the misfit values. This approach aims to show the variance of the results for each inversion run.

Since the scope of this study is to delineate the crustal structure of the region, Moho depth estimates were made for the available stations. The estimates were then classified into different classes according to the sharpness of the discontinuity. Waveforms with the ringing shape often indicate the presence of the sedimentary layers in the shallow crust. With the decreasing velocity, impinging waves become sub-vertical and the conversion between the layers become less effective. This leads to low amplitude, delayed signals and corrupted Moho conversion signature on the waveforms. This type of receiver functions have been observed on several stations. Since it is not possible to constrain the Moho depth from these receiver functions, interpretations were not pursued except marking them as the sedimentary features. The event distribution, merged models for all of the inversion runs and the waveform fits are given for each of the station at figure 3.9-3.32.

The estimated Moho depths for each of the stations are given in table 3.2 with a comment. Results are classified as *sharp*, *intermediate* and *broad*. For some of the stations, Moho estimates were not made due to the sedimentary layer presence.

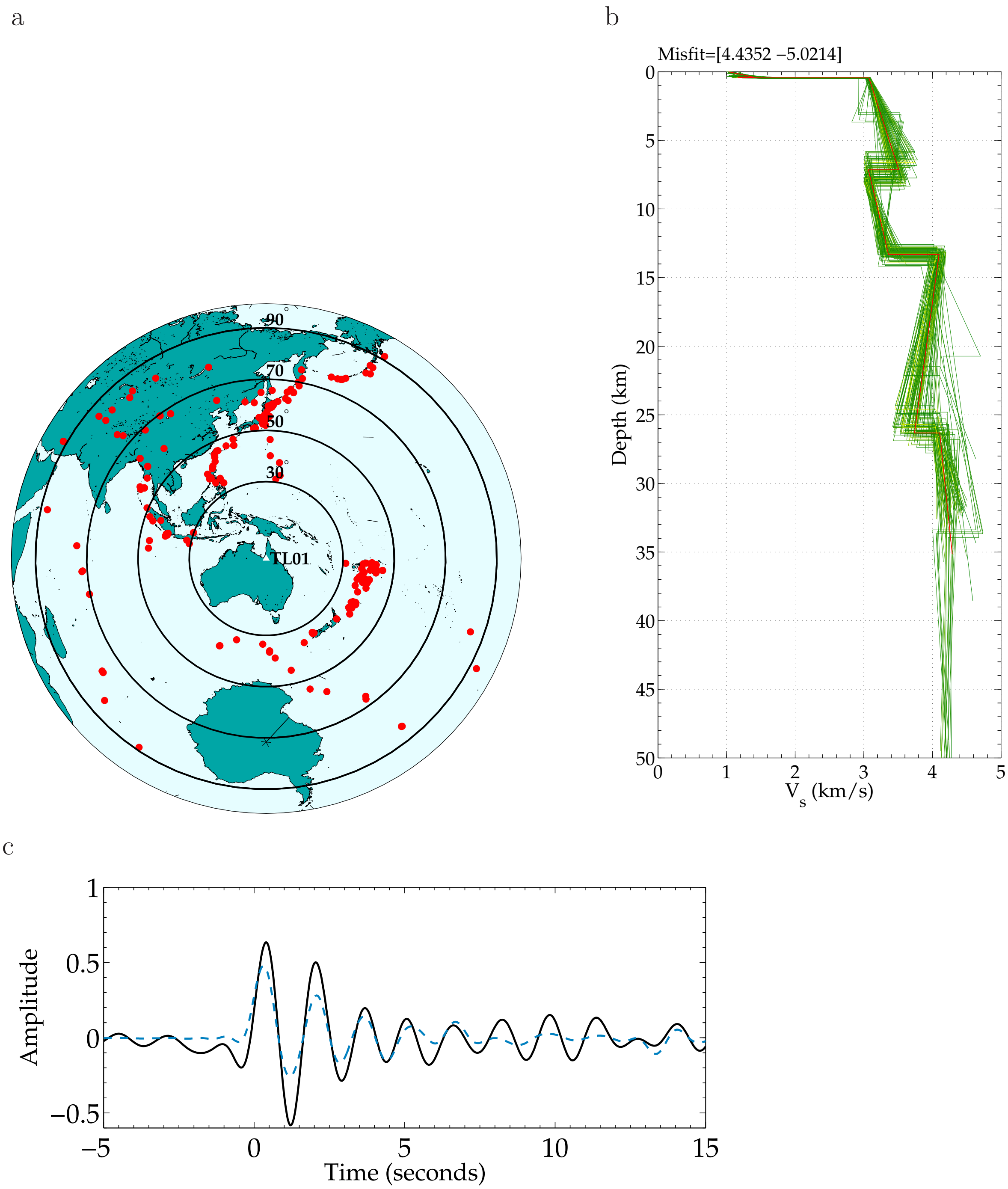

Figure 3.9: a) The distribution of the earthquakes for different distance ranges from TL01. b) Best 100 models and average model (red) from the combination of all inversions. c) The observed (black) and inverted (blue-dashed) receiver functions.

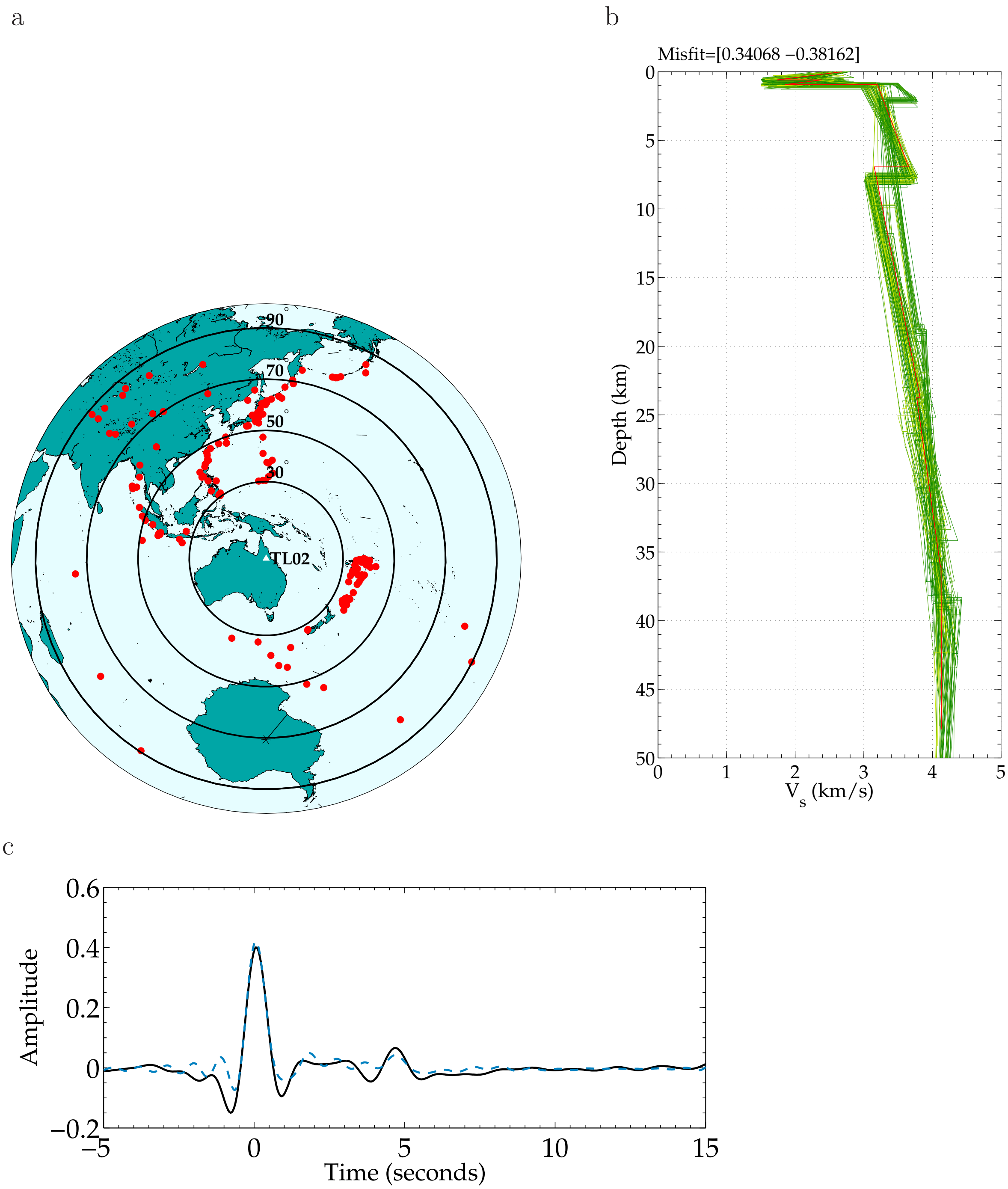

Figure 3.10: a) The distribution of the earthquakes for different distance ranges from TL02. b) Best 100 models and average model (red) from the combination of all inversions. c) The observed (black) and inverted (blue-dashed) radial receiver functions.

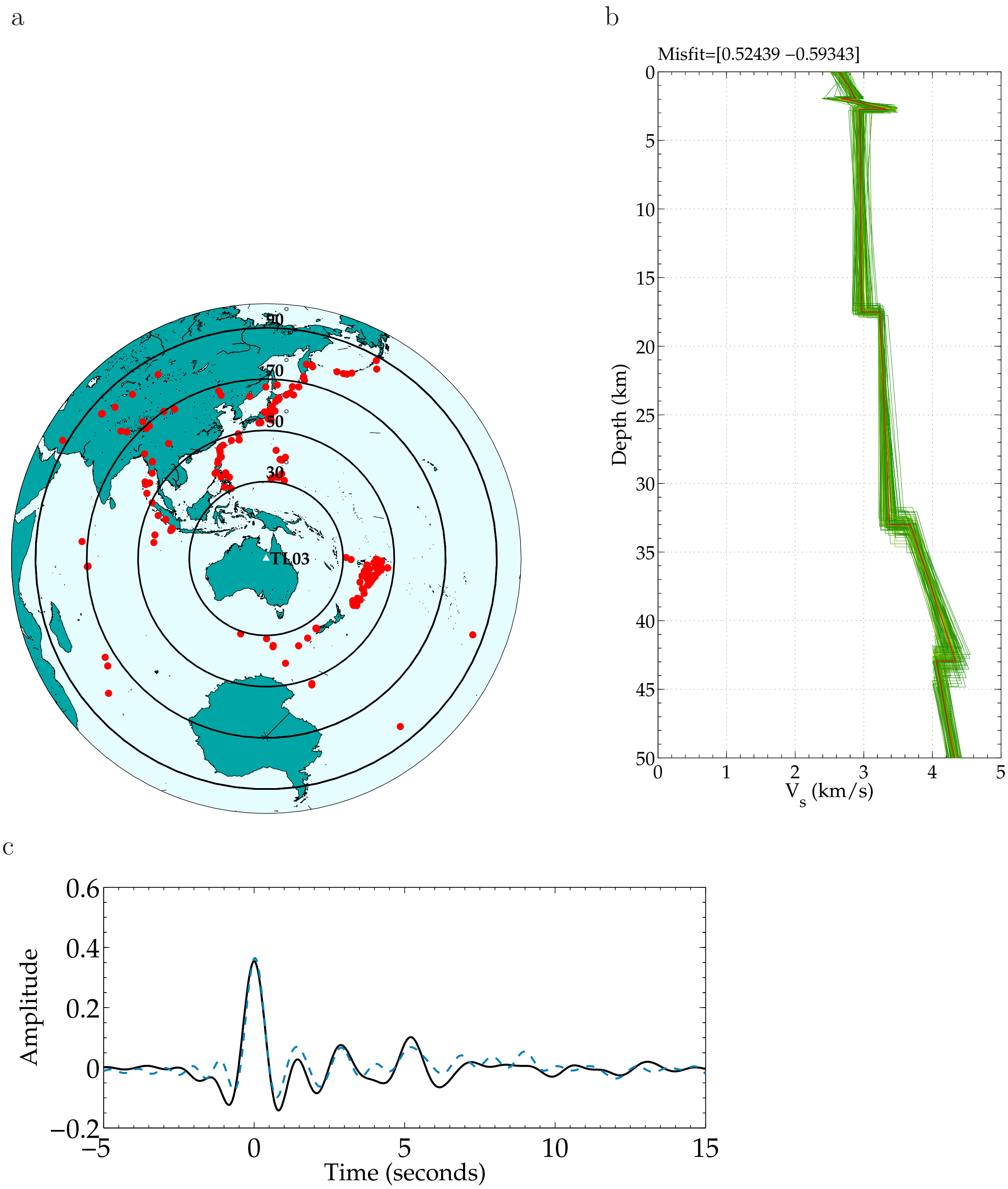

Figure 3.11: a) The distribution of the earthquakes for different distance ranges from TL03. b) Best 100 models and average model (red) from the combination of all inversions. c) The observed (black) and inverted (blue-dashed) radial receiver functions.

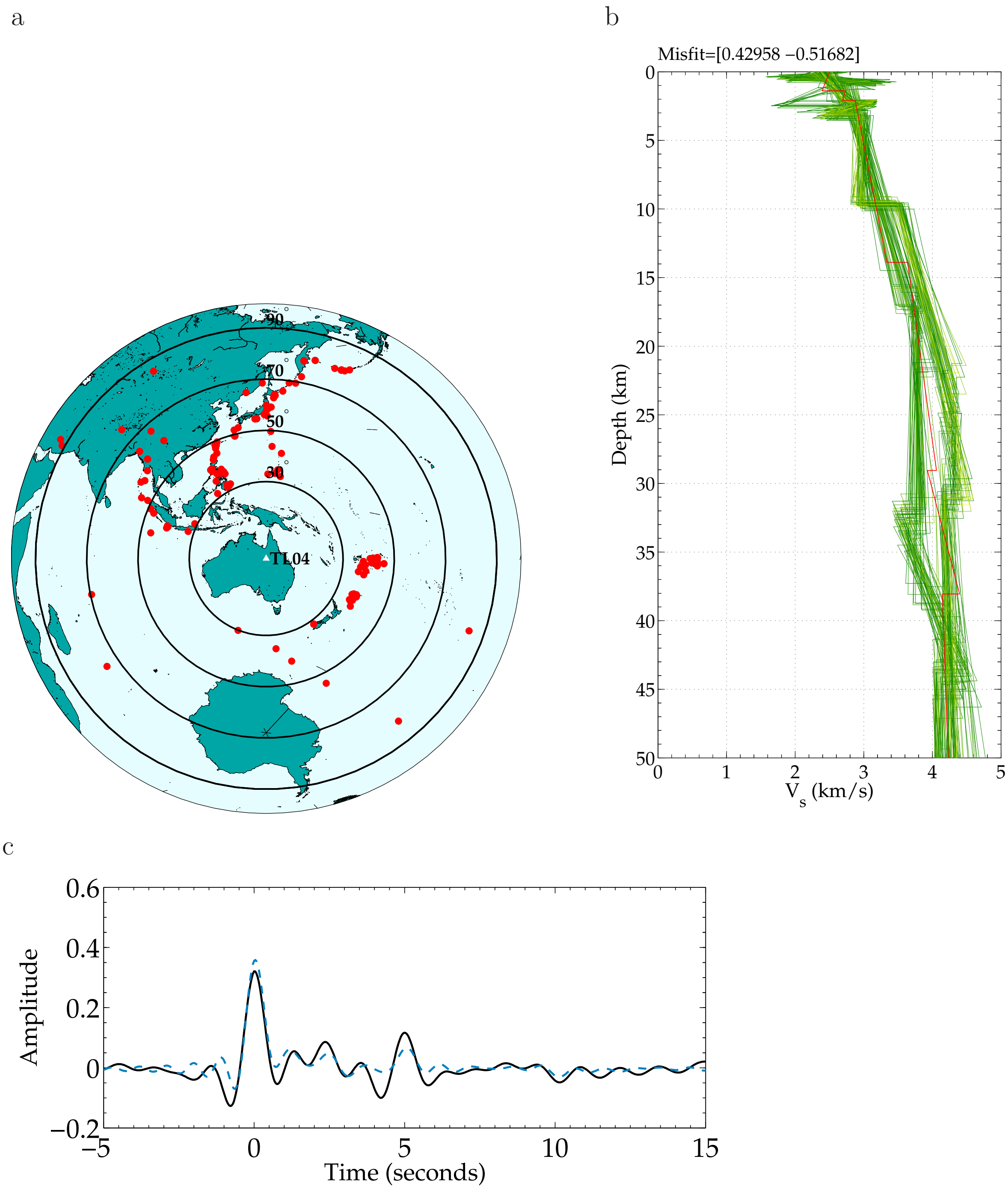

Figure 3.12: a) The distribution of the earthquakes for different distance ranges from TL04. b) Best 100 models and average model (red) from the combination of all inversions. c) The observed (black) and inverted (blue-dashed) radial receiver functions.

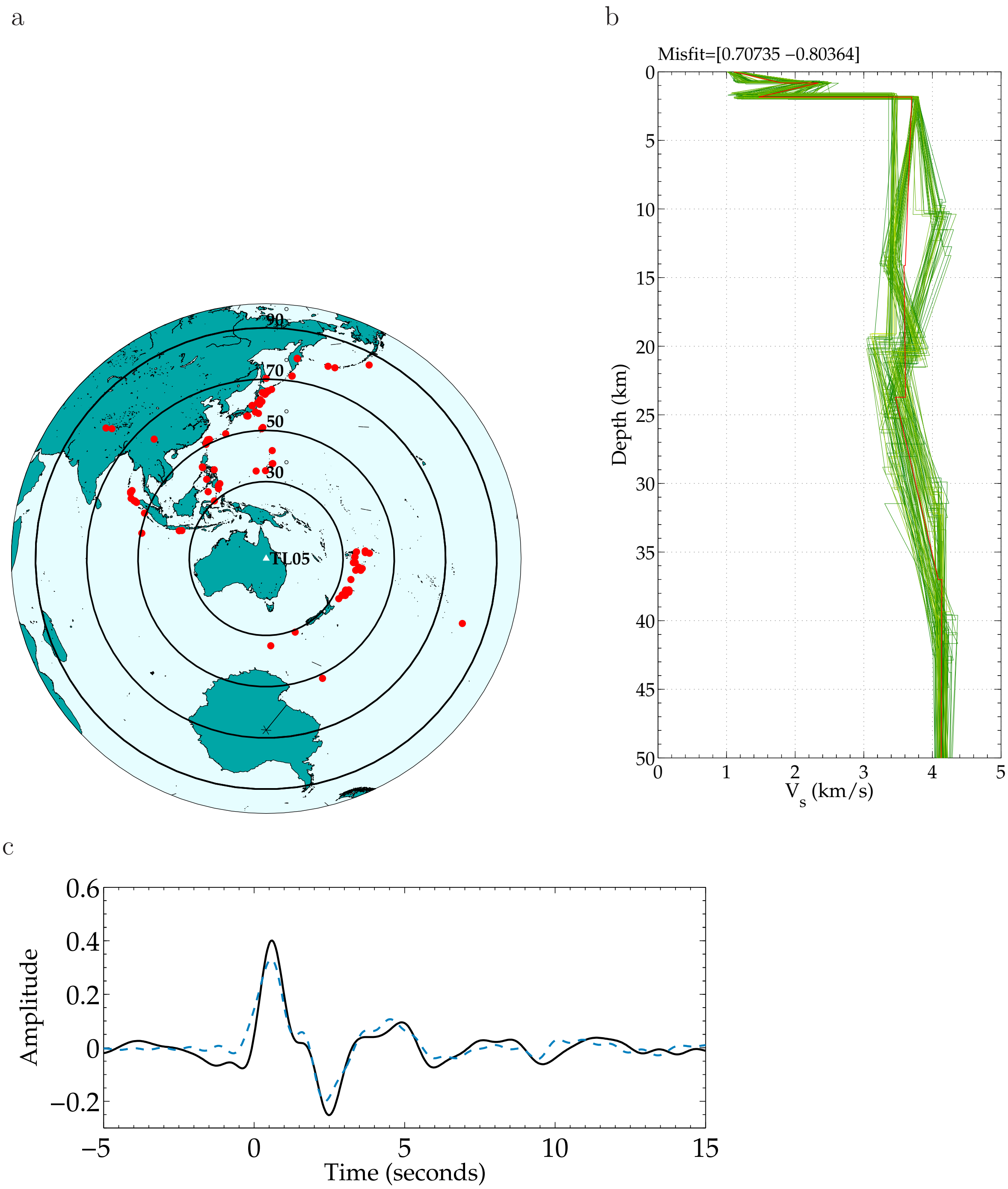

Figure 3.13: a) The distribution of the earthquakes for different distance ranges from TL05. b) Best 100 models and average model (red) from the combination of all inversions. c) The observed (black) and inverted (blue-dashed) radial receiver functions.

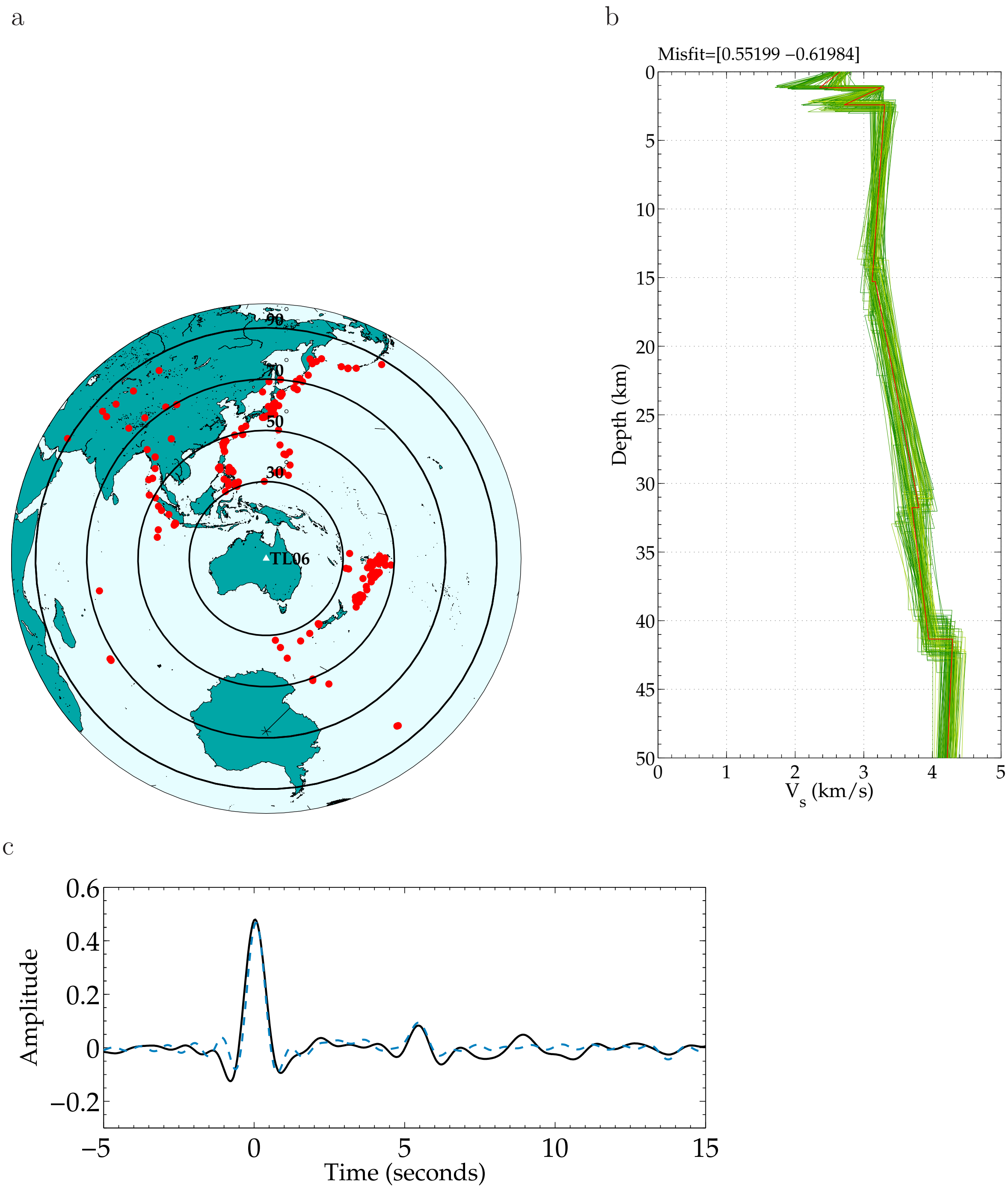

Figure 3.14: a) The distribution of the earthquakes for different distance ranges from TL06. b) Best 100 models and average model (red) from the combination of all inversions. c) The observed (black) and inverted (blue-dashed) radial receiver functions.

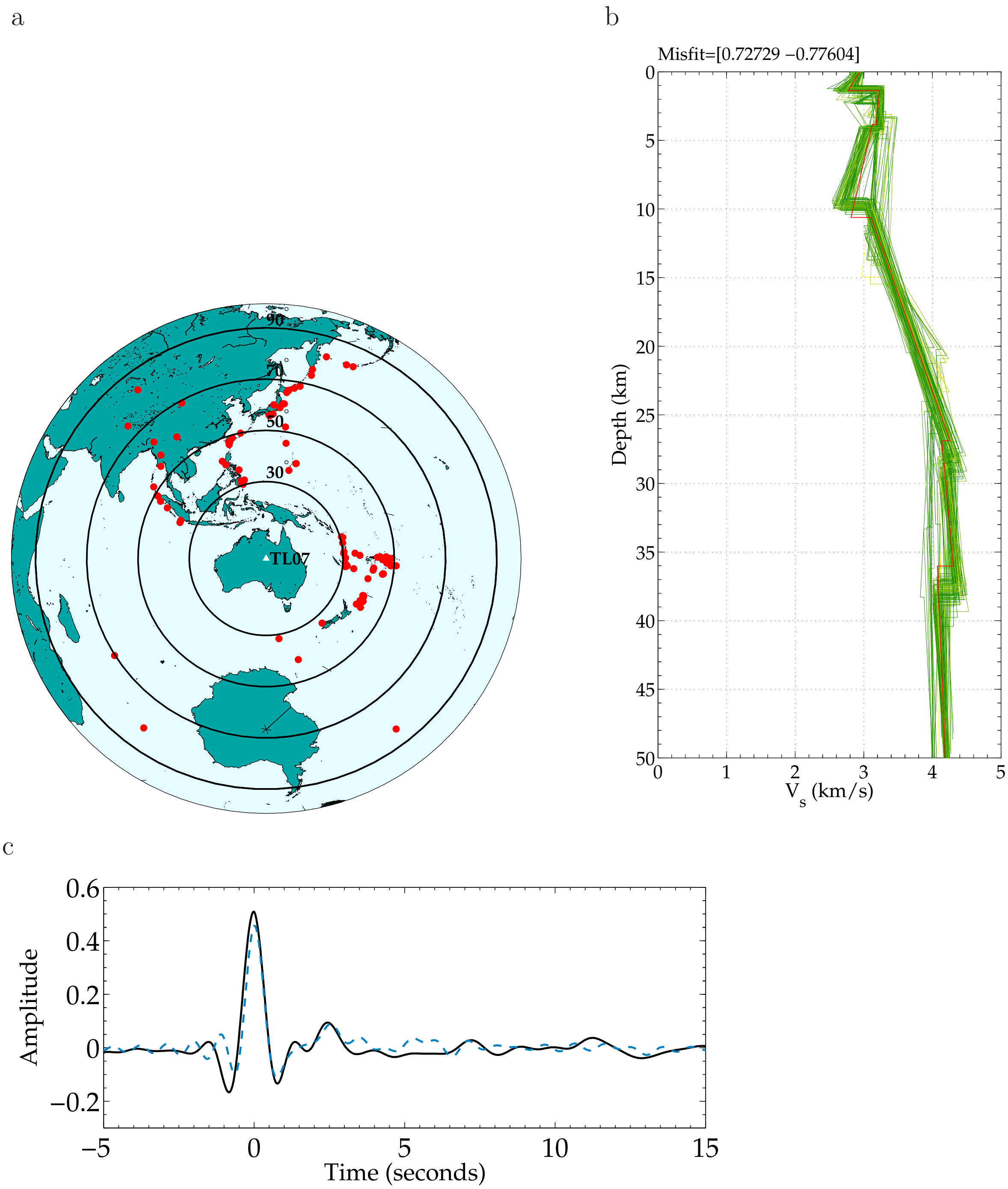

Figure 3.15: a) The distribution of the earthquakes for different distance ranges from TL07. b) Best 100 models from the combination of all inversions. c) The observed (black) and inverted (blue-dashed) radial receiver functions.

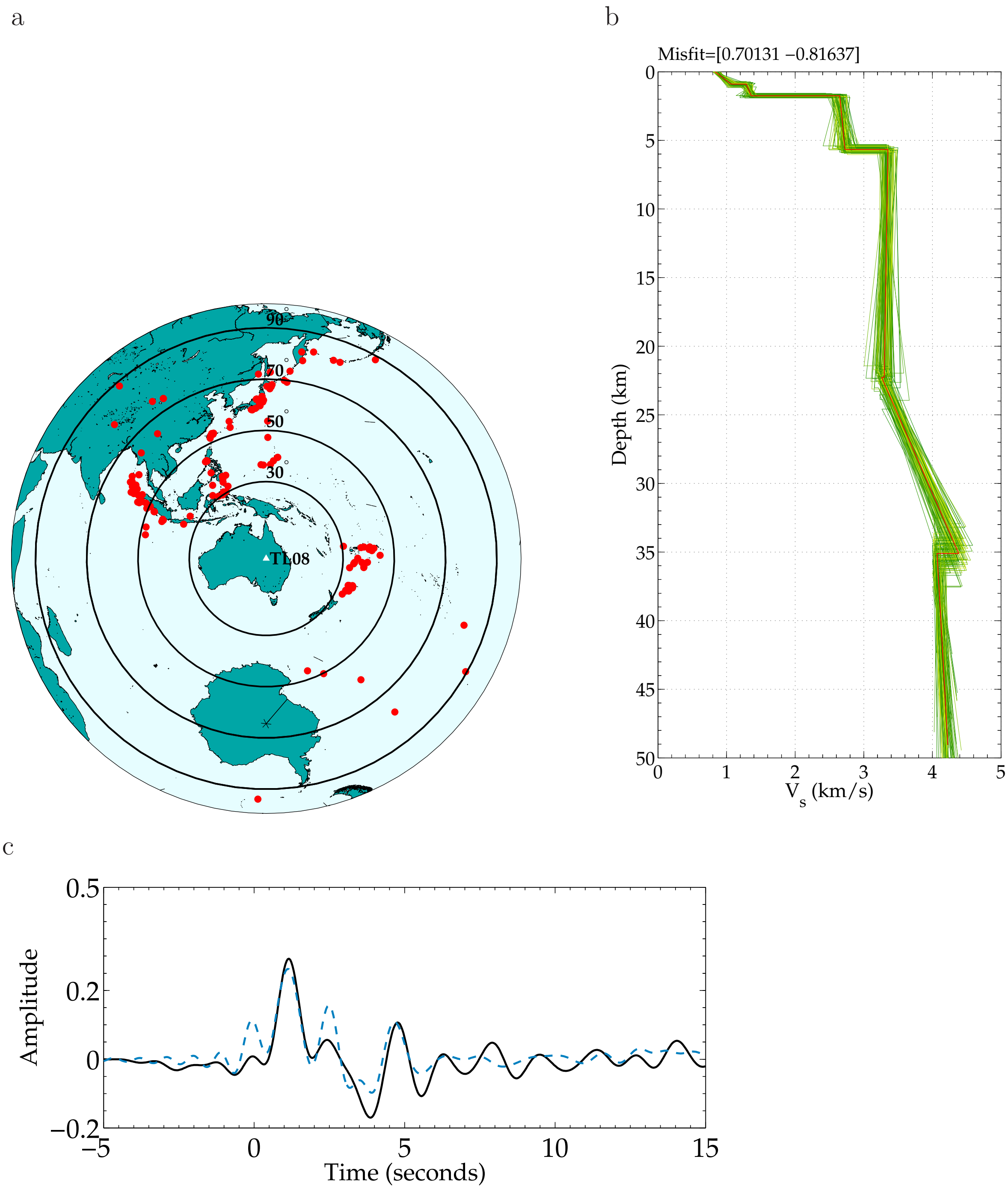

Figure 3.16: a) The distribution of the earthquakes for different distance ranges from TL08. b) Best 100 models and average model (red) from the combination of all inversions. c) The observed (black) and inverted (blue-dashed) radial receiver functions.

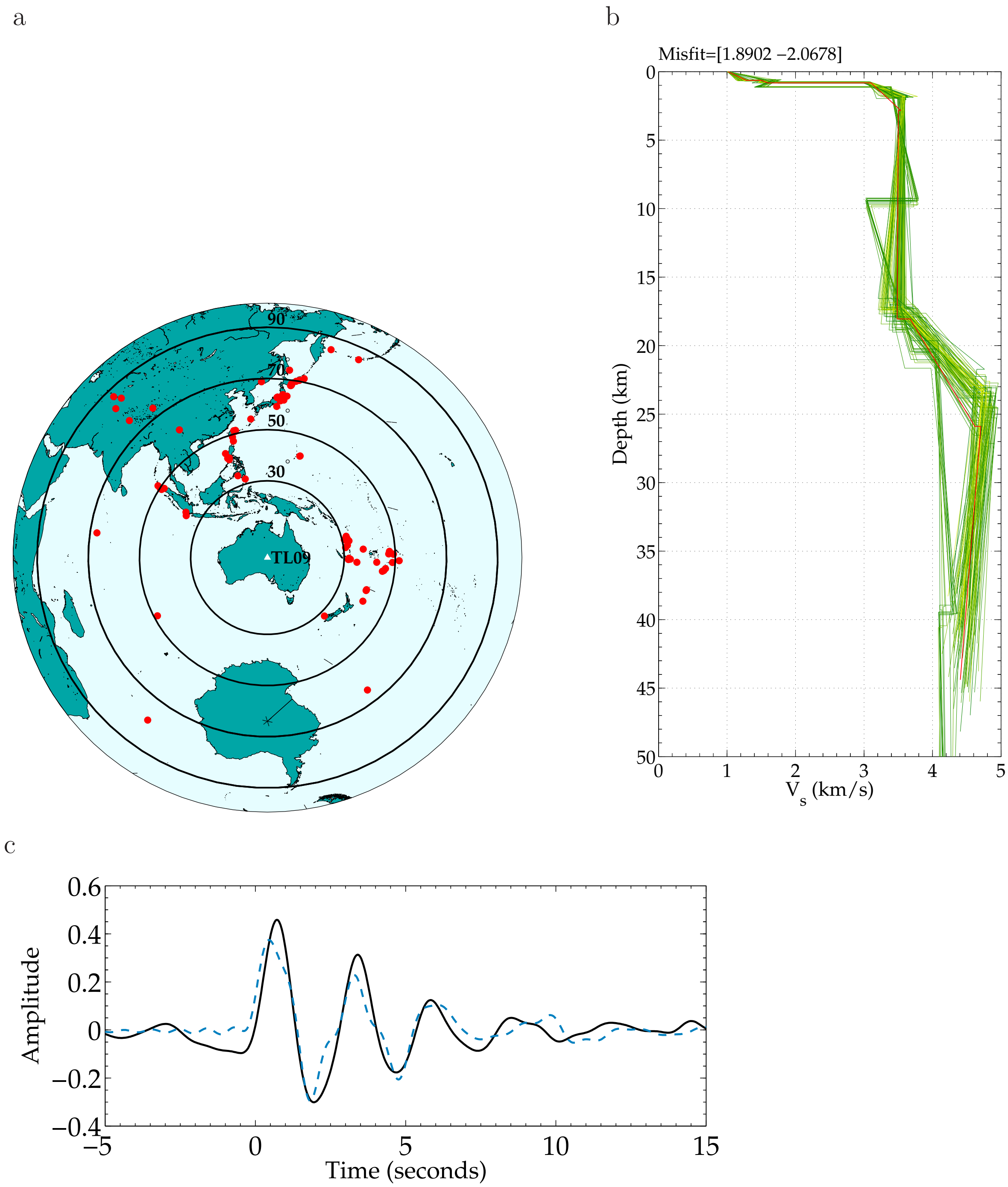

Figure 3.17: a) The distribution of the earthquakes for different distance ranges from TL09. b) Best 100 models and average model (red) from the combination of all inversions. c) The observed (black) and inverted (blue-dashed) radial receiver functions.

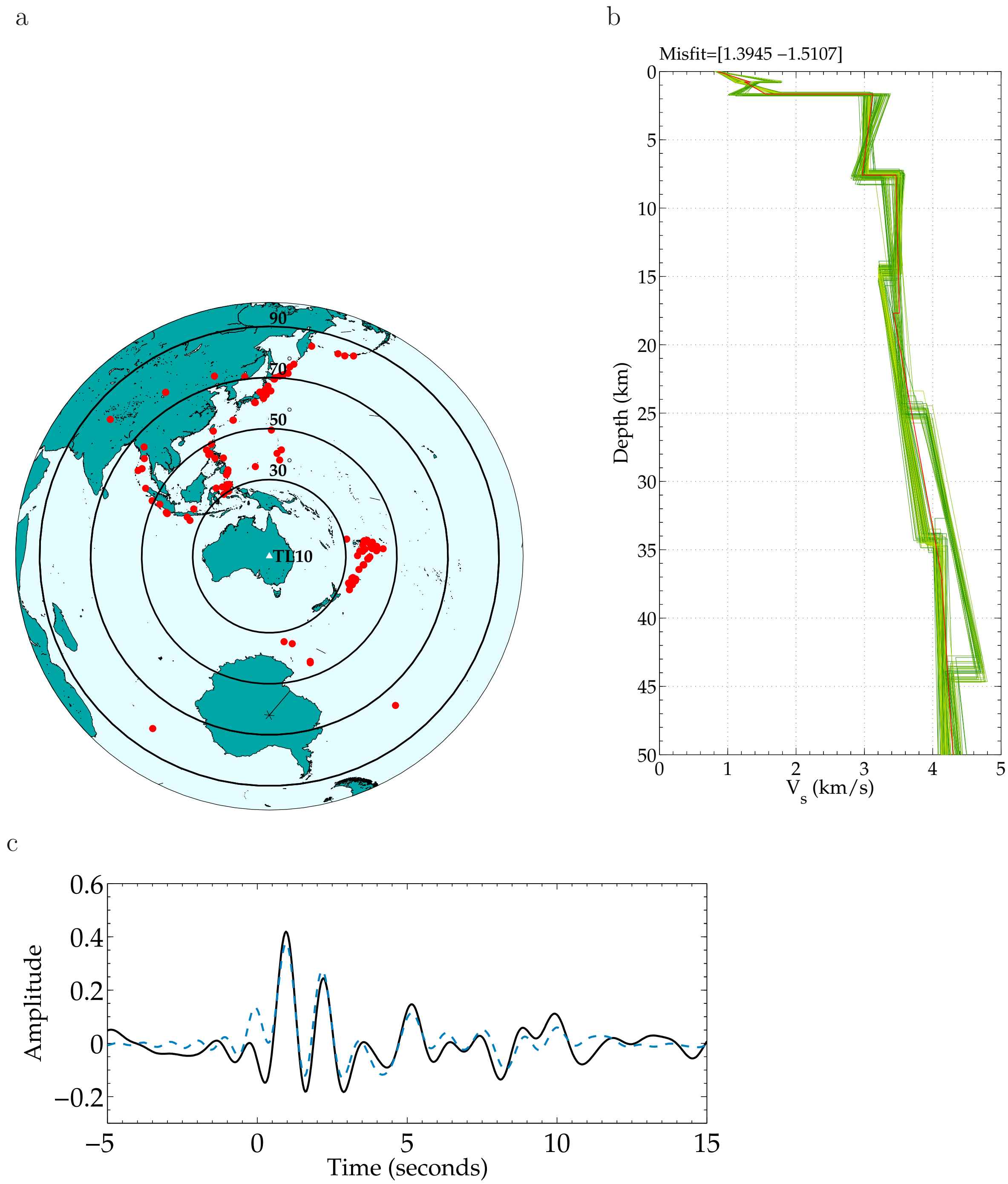

Figure 3.18: a) The distribution of the earthquakes for different distance ranges from TL10. b) Best 100 models and average model (red) from the combination of all inversions. c) The observed (black) and inverted (blue-dashed) radial receiver functions.

a

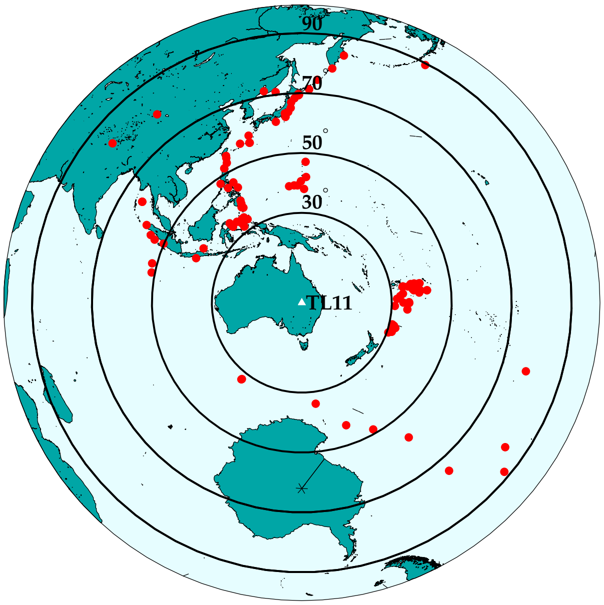

b

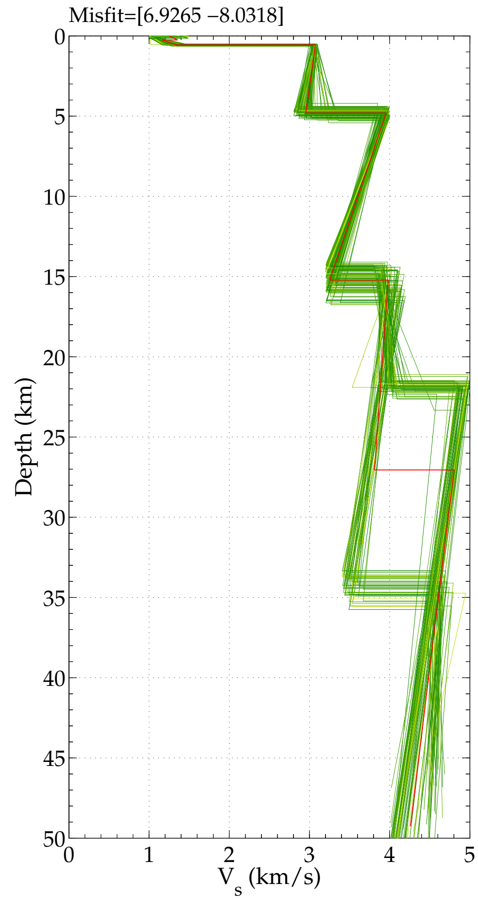

c

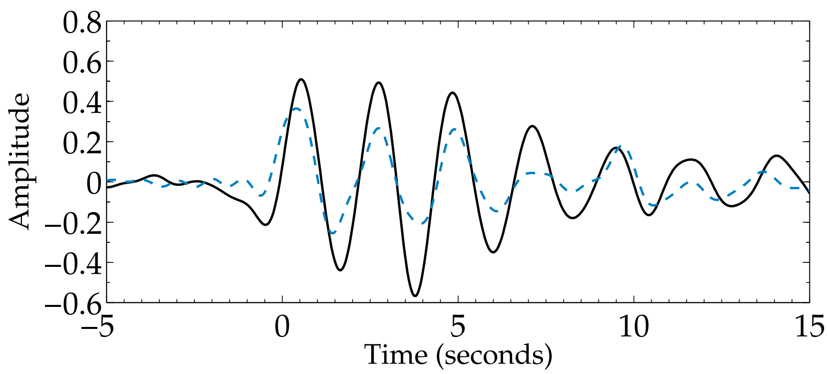

Figure 3.19: a) The distribution of the earthquakes for different distance ranges from TL11. b) Best 100 models and average model (red) from the combination of all inversions. c) The observed (black) and inverted (blue-dashed) radial receiver functions.

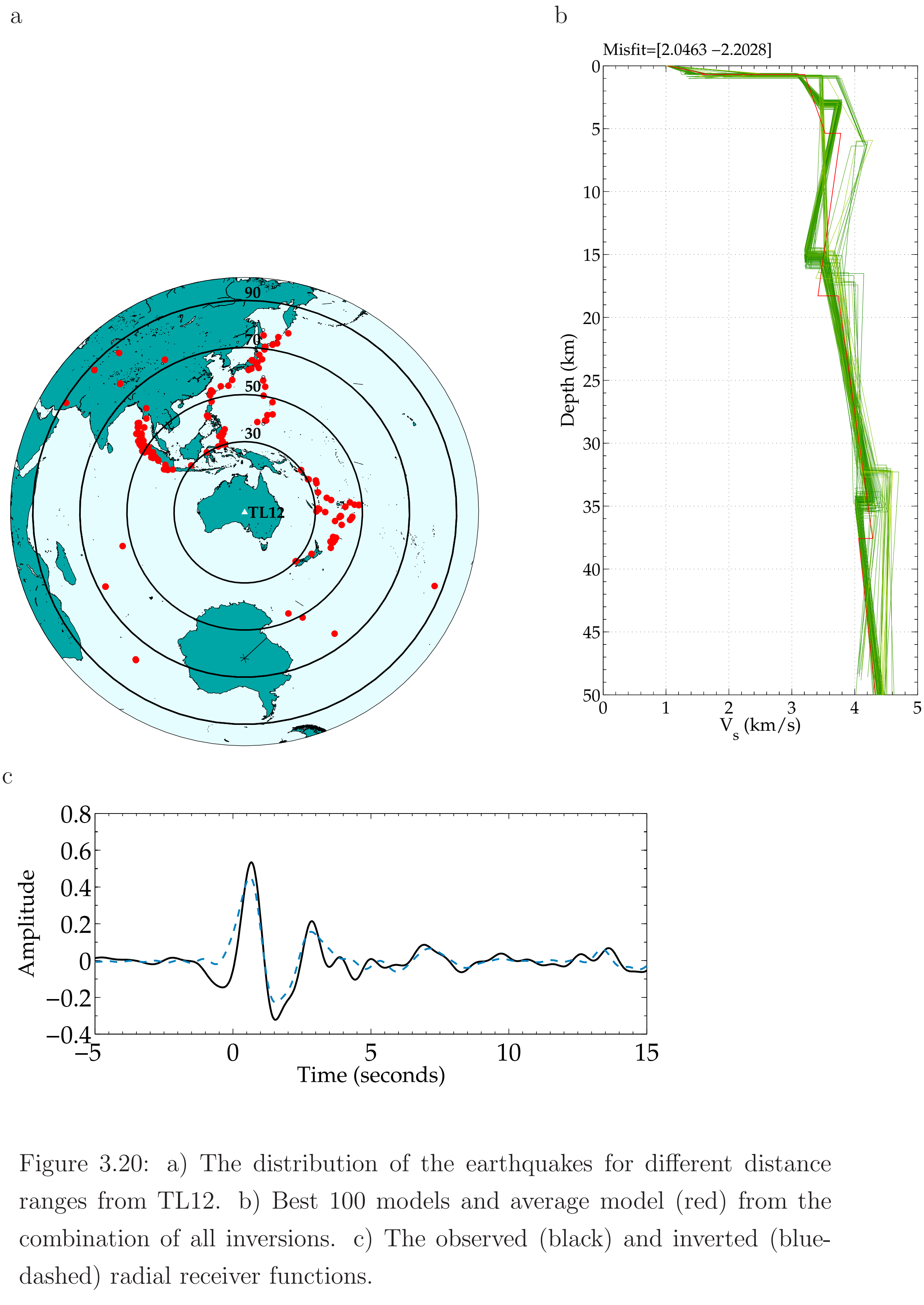

Figure 3.20: a) The distribution of the earthquakes for different distance ranges from TL12. b) Best 100 models and average model (red) from the combination of all inversions. c) The observed (black) and inverted (blue-dashed) radial receiver functions.

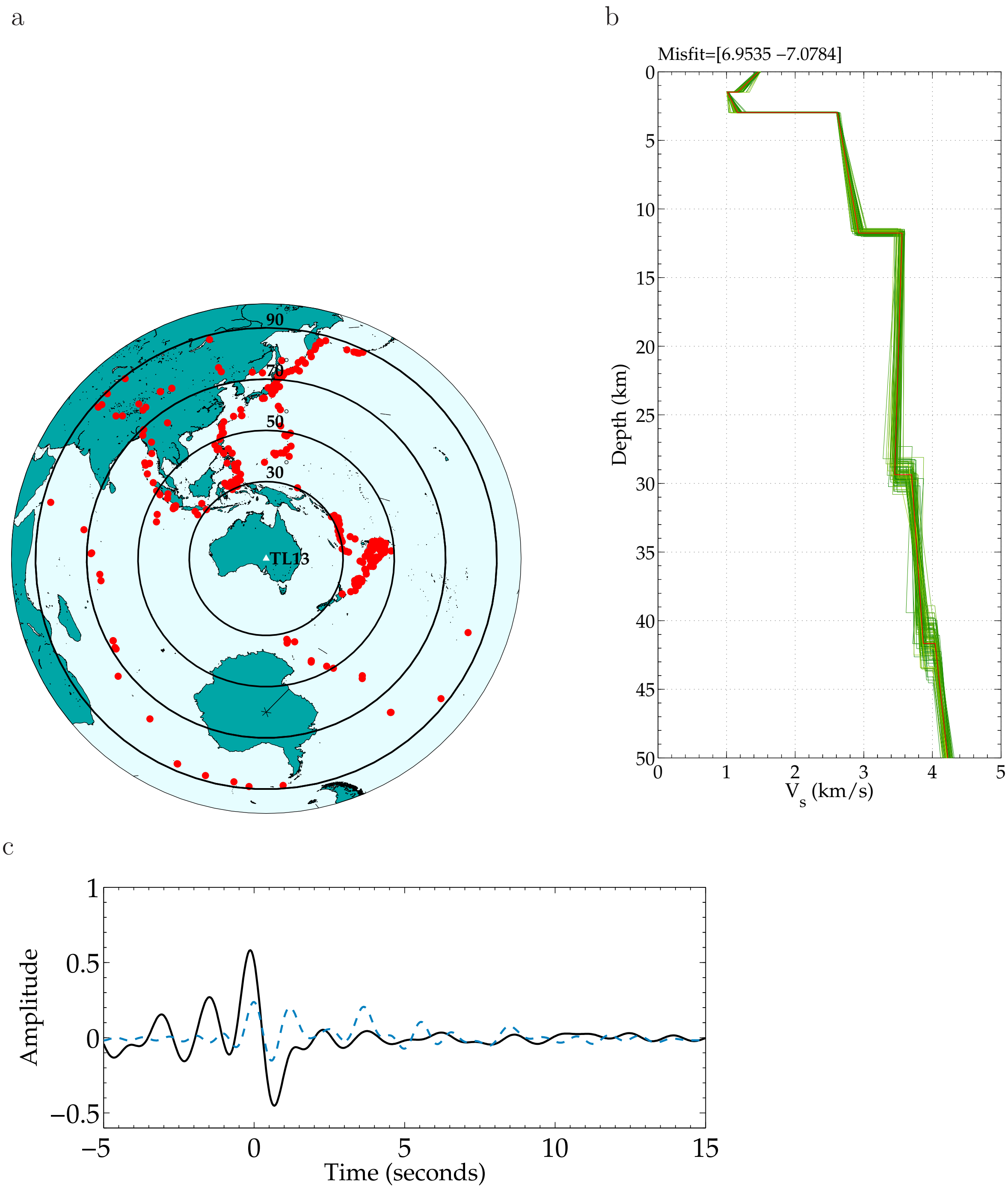

Figure 3.21: a) The distribution of the earthquakes for different distance ranges from TL13. b) Best 100 models and average model (red) from the combination of all inversions. c) The observed (black) and inverted (blue-dashed) radial receiver functions.

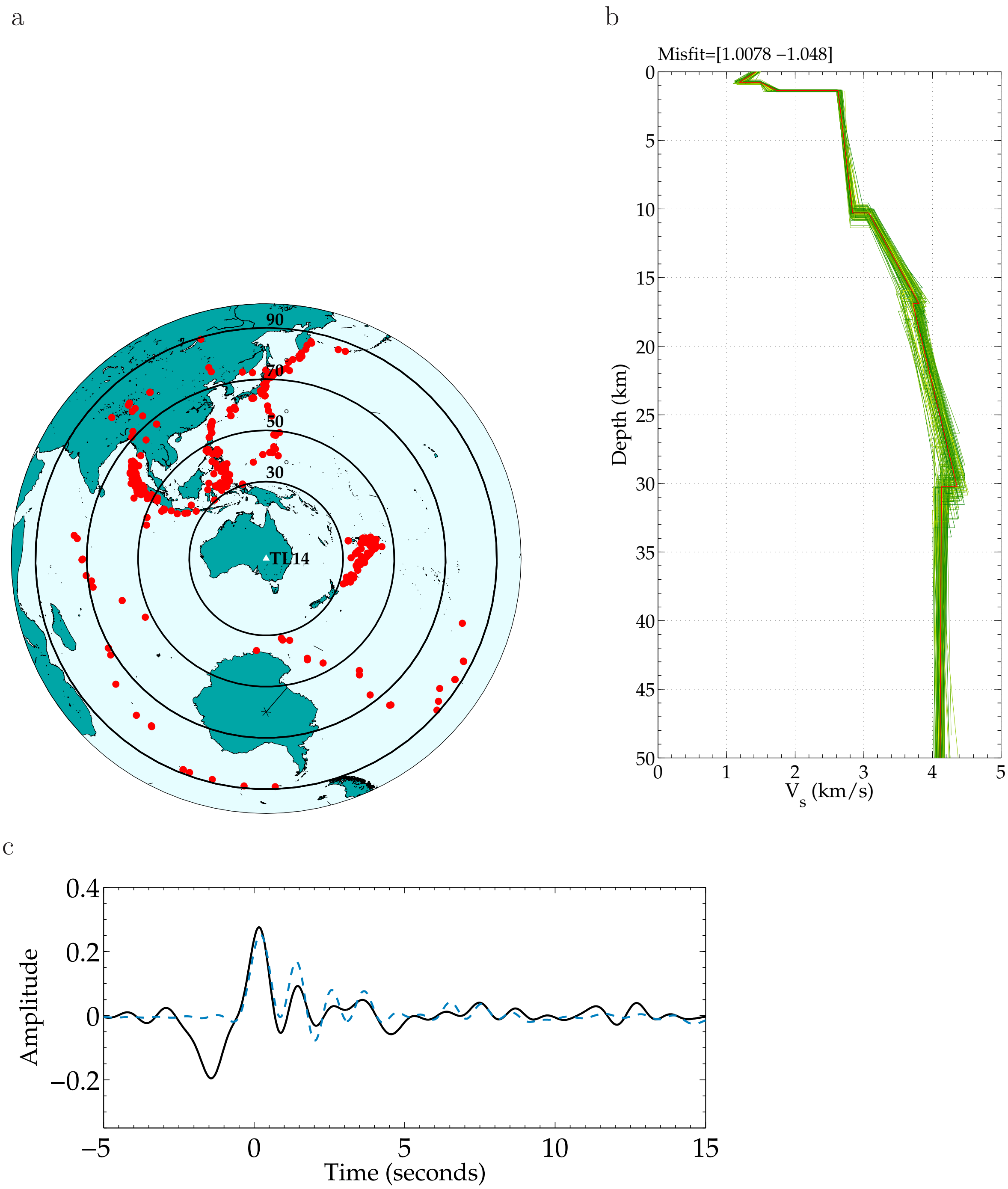

Figure 3.22: a) The distribution of the earthquakes for different distance ranges from TL14. b) Best 100 models and average model (red) from the combination of all inversions. c) The observed (black) and inverted (blue-dashed) radial receiver functions.

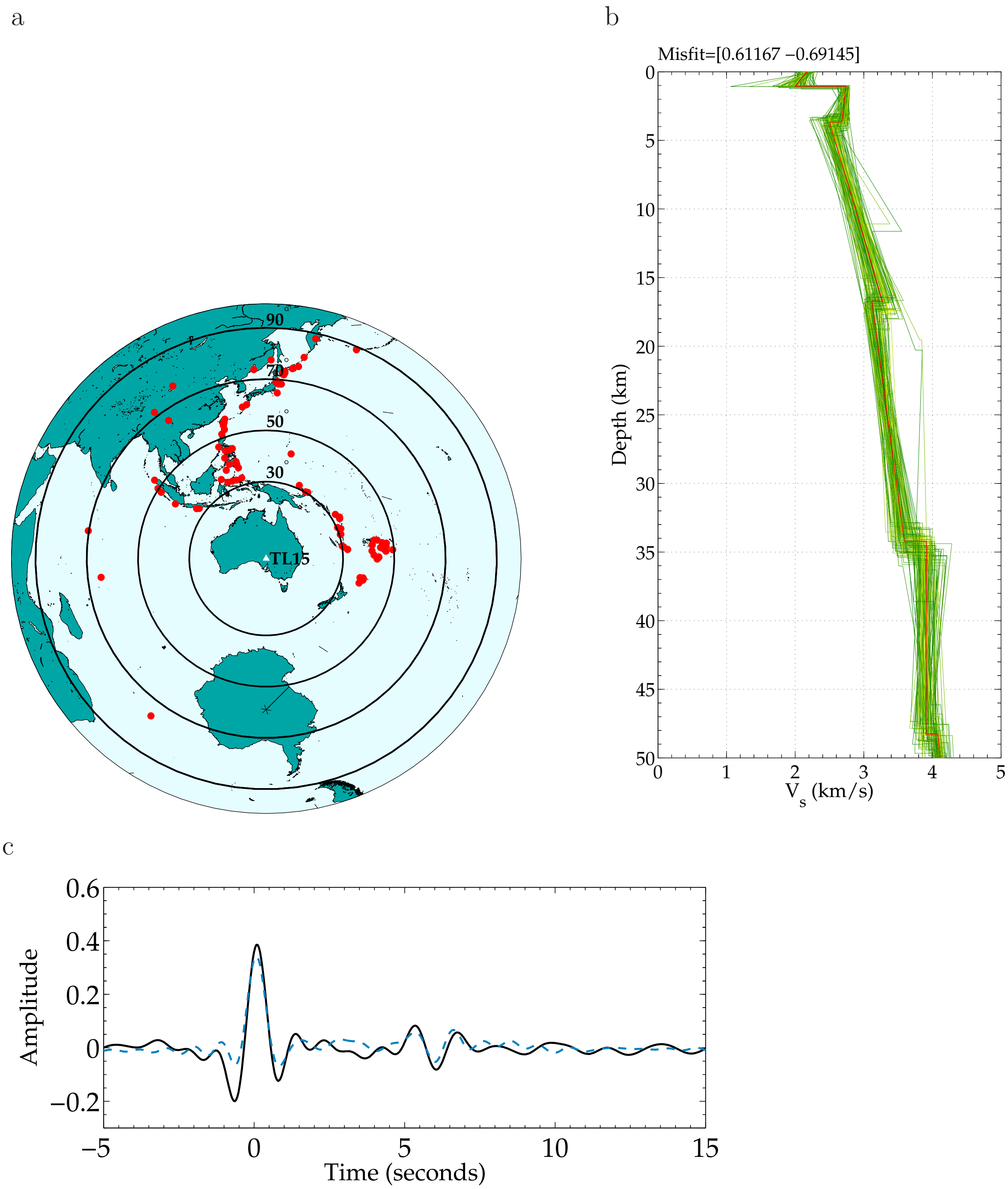

Figure 3.23: a) The distribution of the earthquakes for different distance ranges from TL15. b) Best 100 models and average model (red) from the combination of all inversions. c) The observed (black) and inverted (blue-dashed) radial receiver functions.

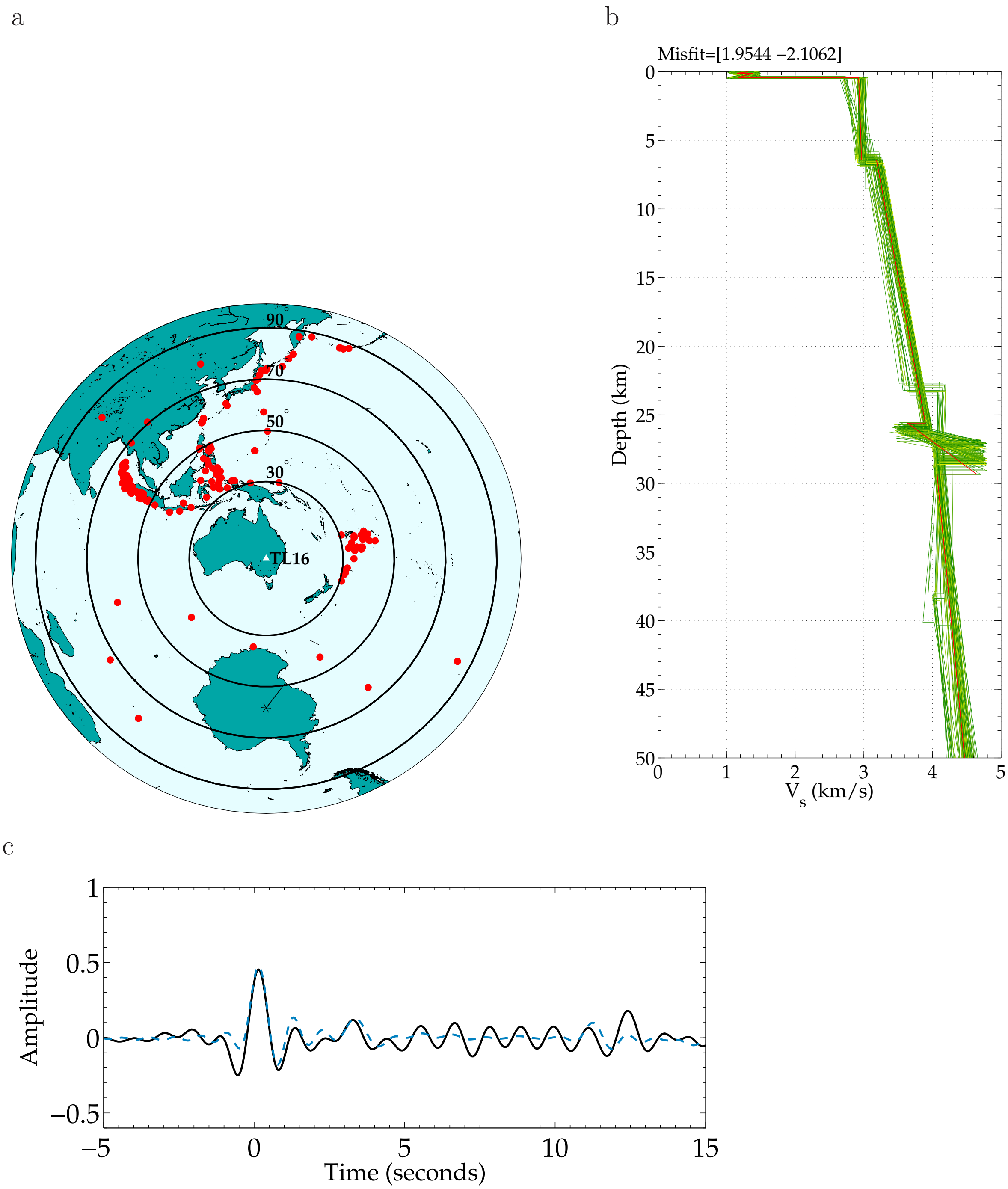

Figure 3.24: a) The distribution of the earthquakes for different distance ranges from TL16. b) Best 100 models and average model (red) from the combination of all inversions. c) The observed (black) and inverted (blue-dashed) radial receiver functions.

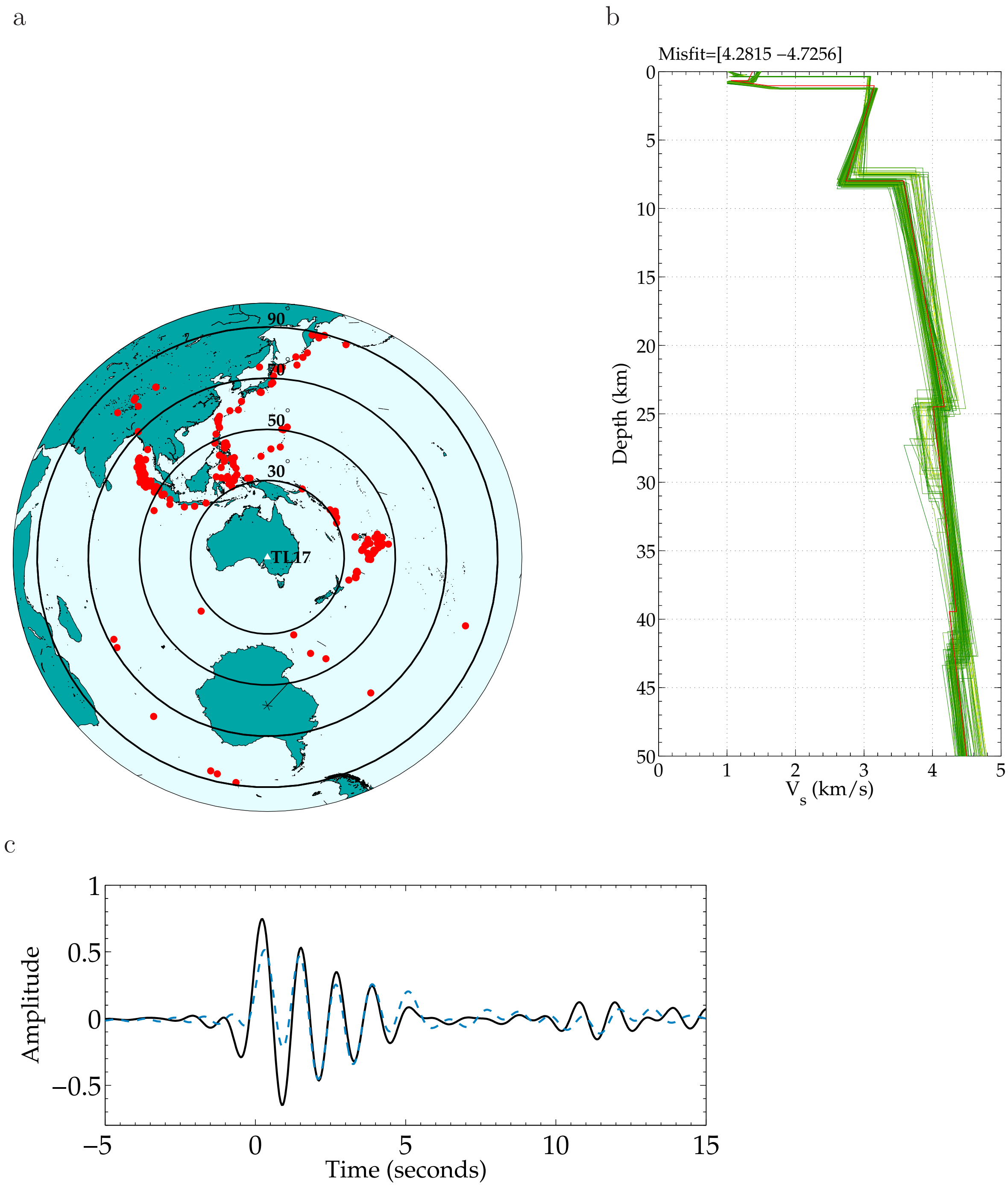

Figure 3.25: a) The distribution of the earthquakes for different distance ranges from TL17. b) Best 100 models and average model (red) from the combination of all inversions. c) The observed (black) and inverted (blue-dashed) radial receiver functions.

a

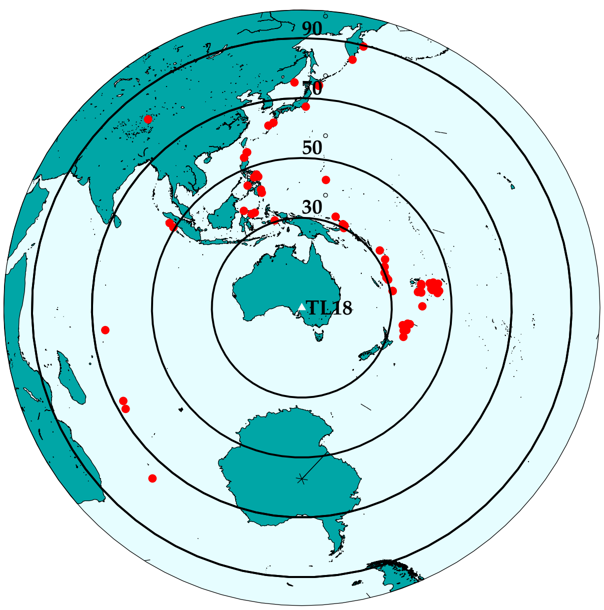

b

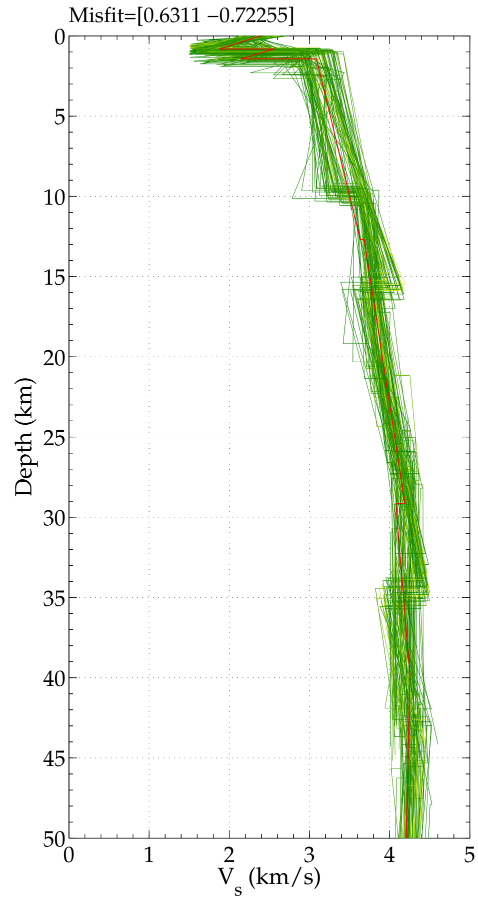

c

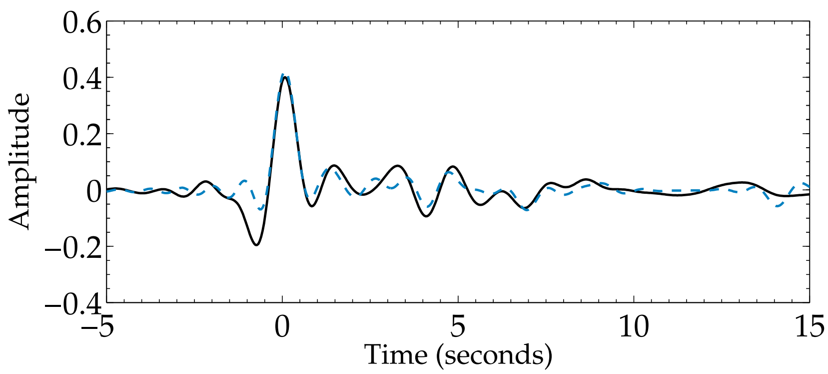

Figure 3.26: a) The distribution of the earthquakes for different distance ranges from TL18. b) Best 100 models and average model (red) from the combination of all inversions. c) The observed (black) and inverted (blue-dashed) radial receiver functions.

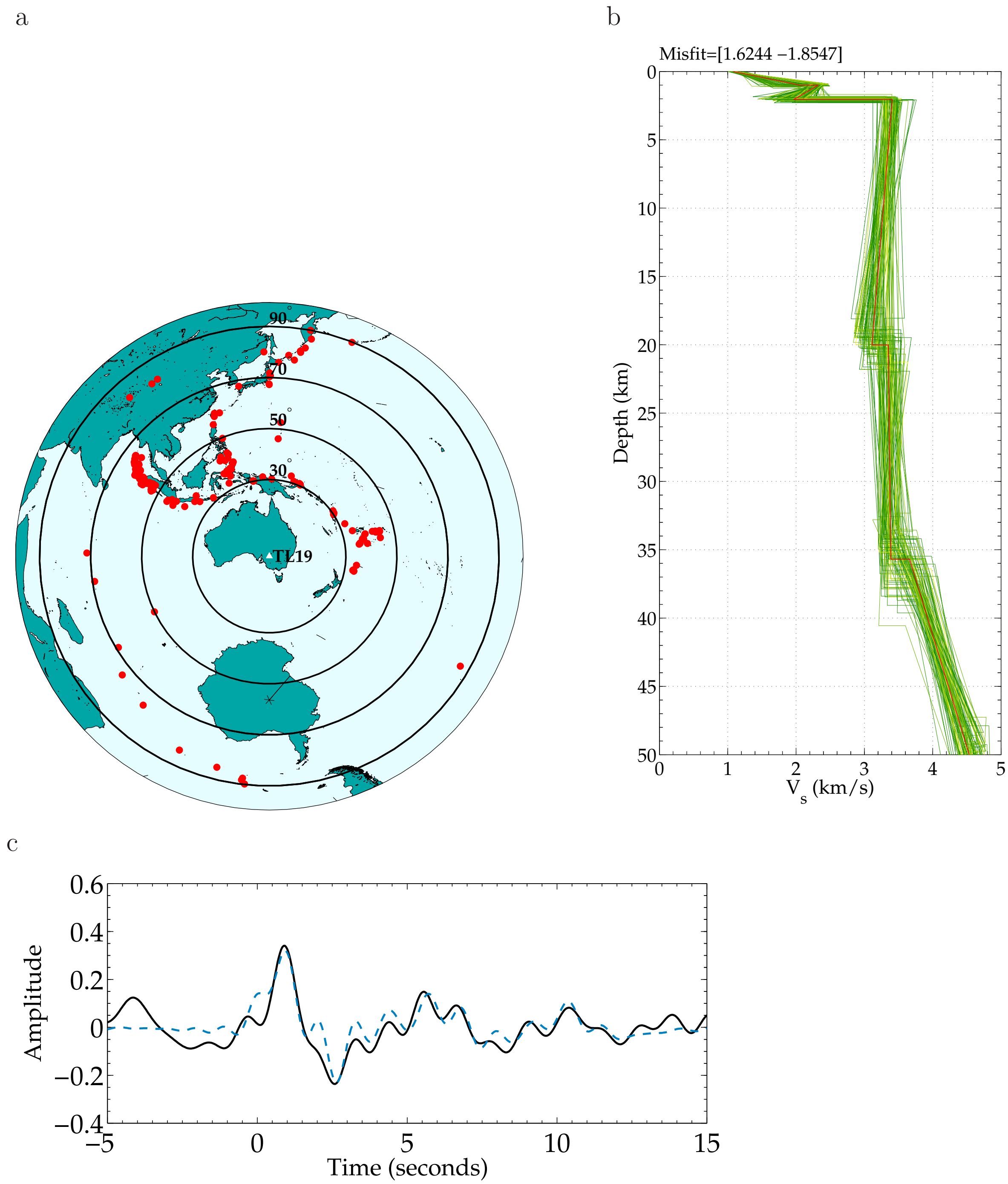

Figure 3.27: a) The distribution of the earthquakes for different distance ranges from TL19. b) Best 100 models and average model (red) from the combination of all inversions. c) The observed (black) and inverted (blue-dashed) radial receiver functions.

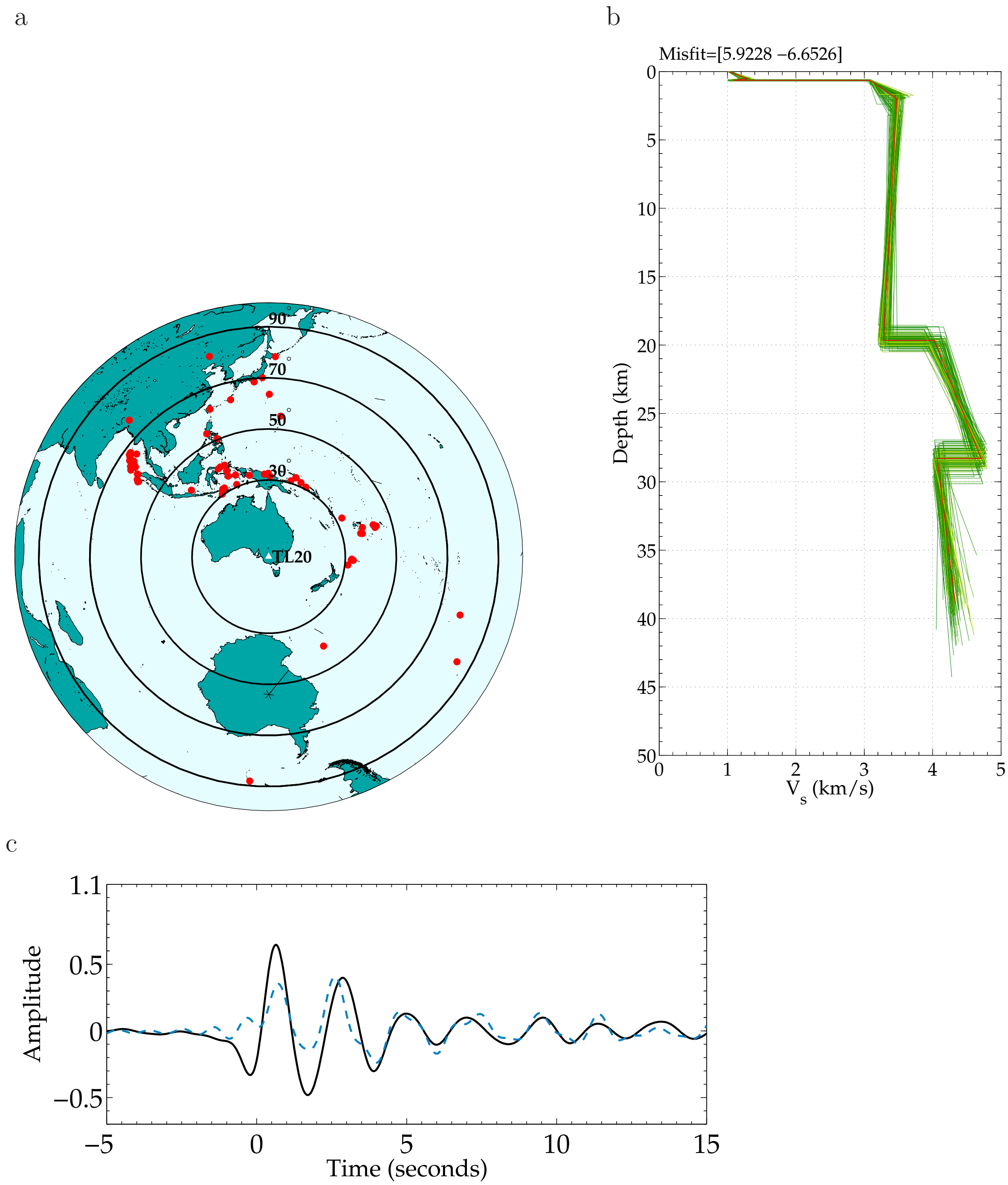

Figure 3.28: a) The distribution of the earthquakes for different distance ranges from TL20. b) Best 100 models and average model (red) from the combination of all inversions. c) The observed (black) and inverted (blue-dashed) radial receiver functions.

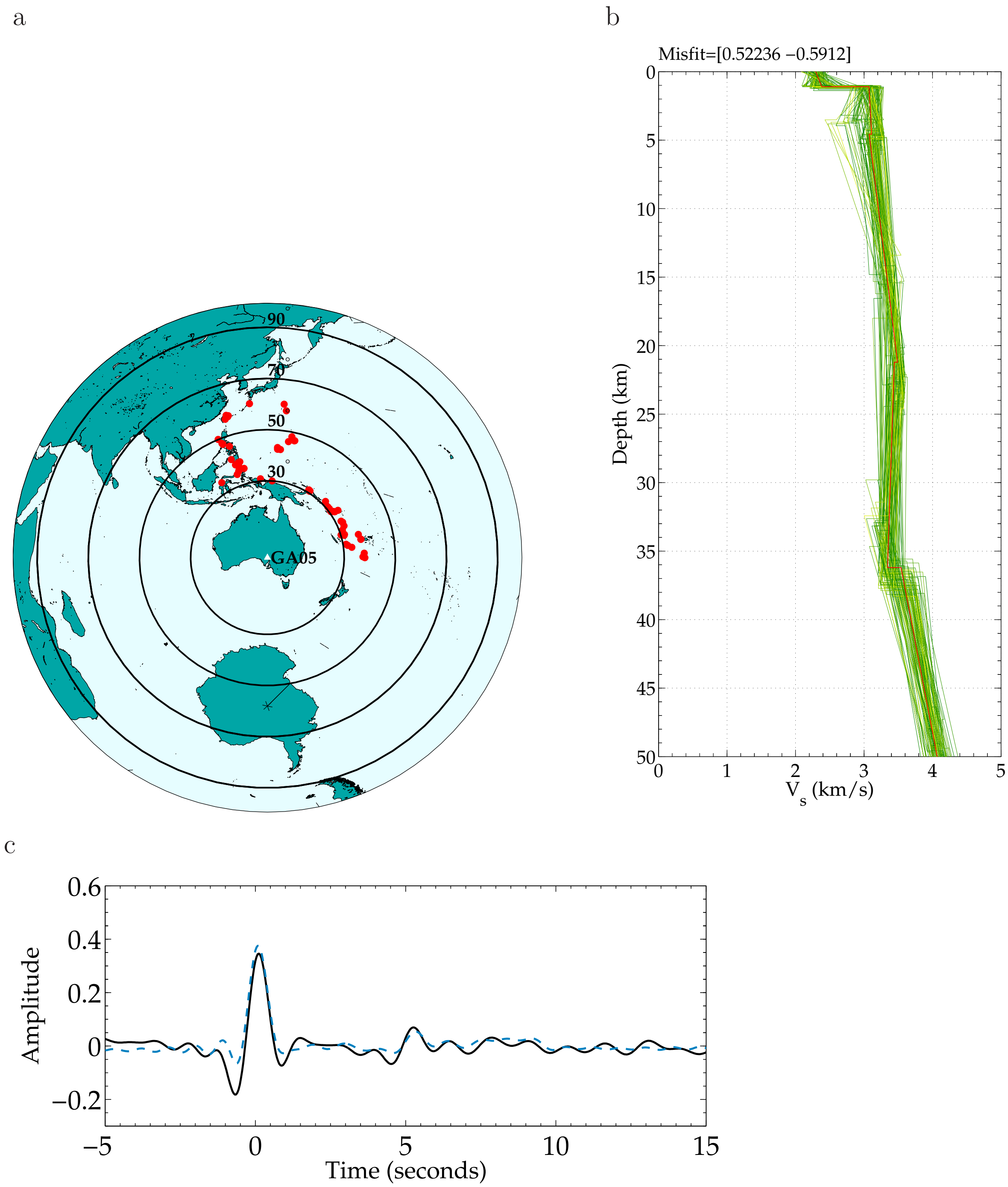

Figure 3.29: a) The distribution of the earthquakes for different distance ranges from GA05. b) Best 100 models and average model (red) from the combination of all inversions. c) The observed (black) and inverted (blue-dashed) radial receiver functions.

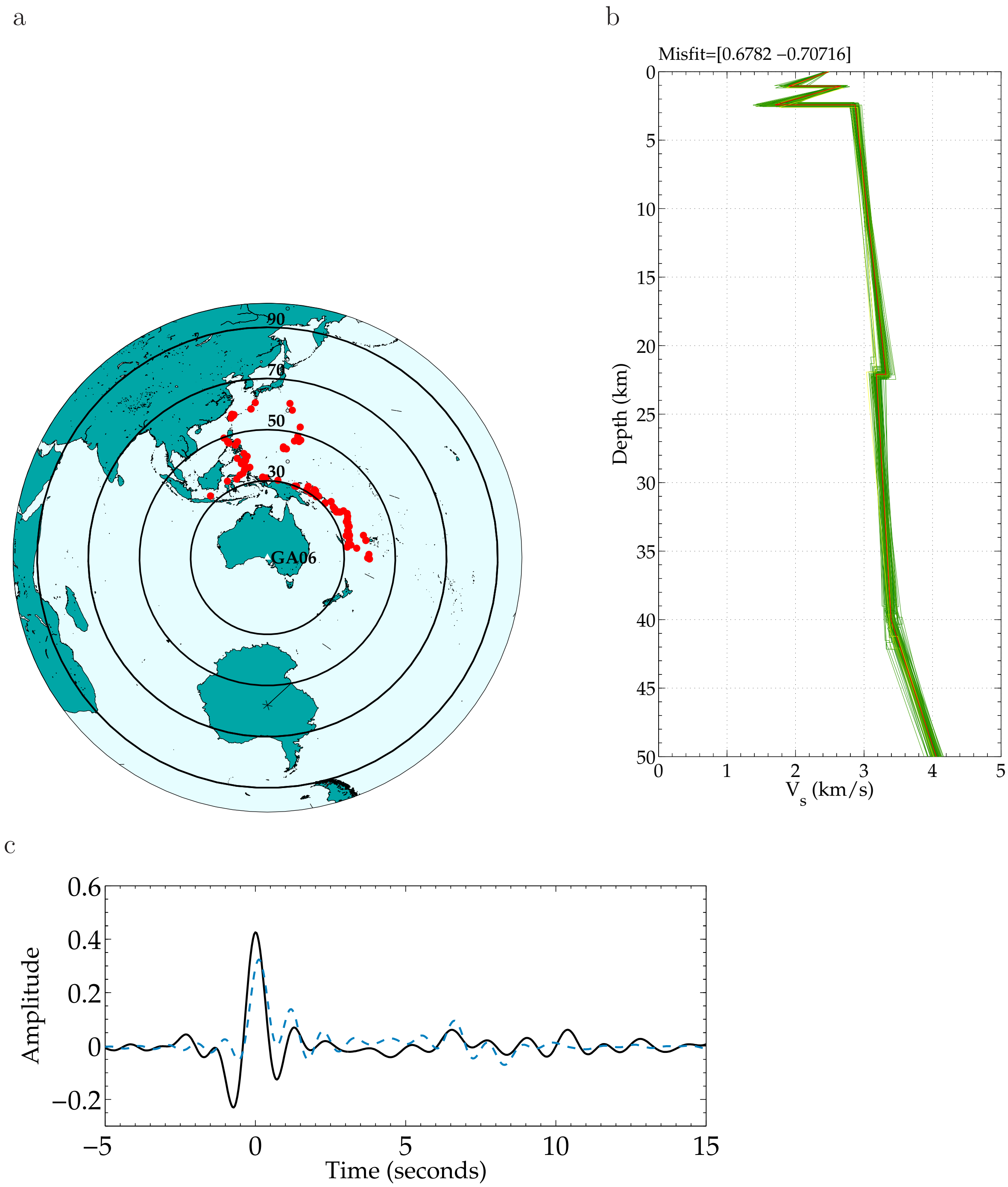

Figure 3.30: a) The distribution of the earthquakes for different distance ranges from GA06. b) Best 100 models and average model (red) from the combination of all inversions. c) The observed (black) and inverted (blue-dashed) radial receiver functions.

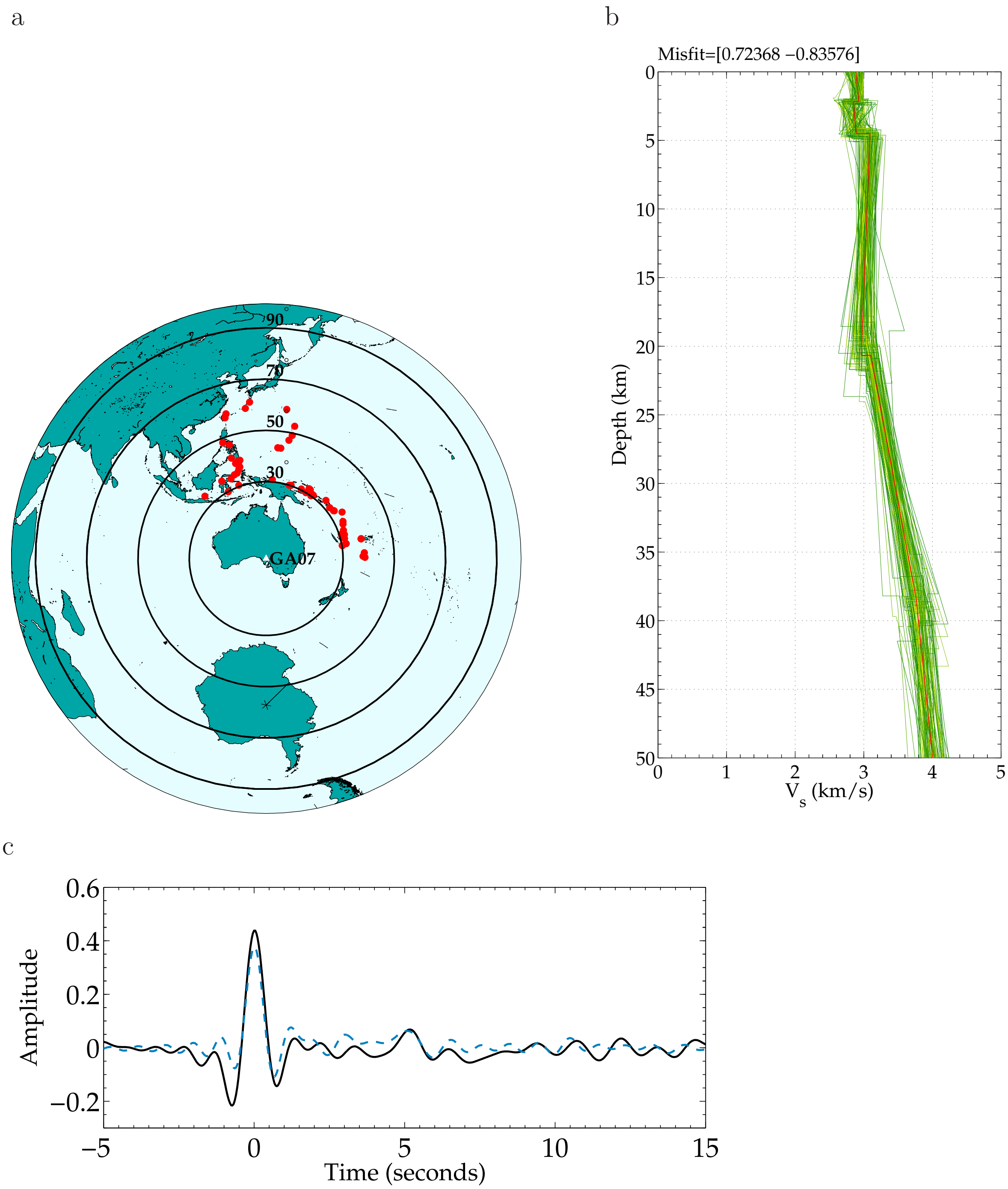

Figure 3.31: a) The distribution of the earthquakes for different distance ranges from GA07. b) Best 100 models and average model (red) from the combination of all inversions. c) The observed (black) and inverted (blue-dashed) radial receiver functions.

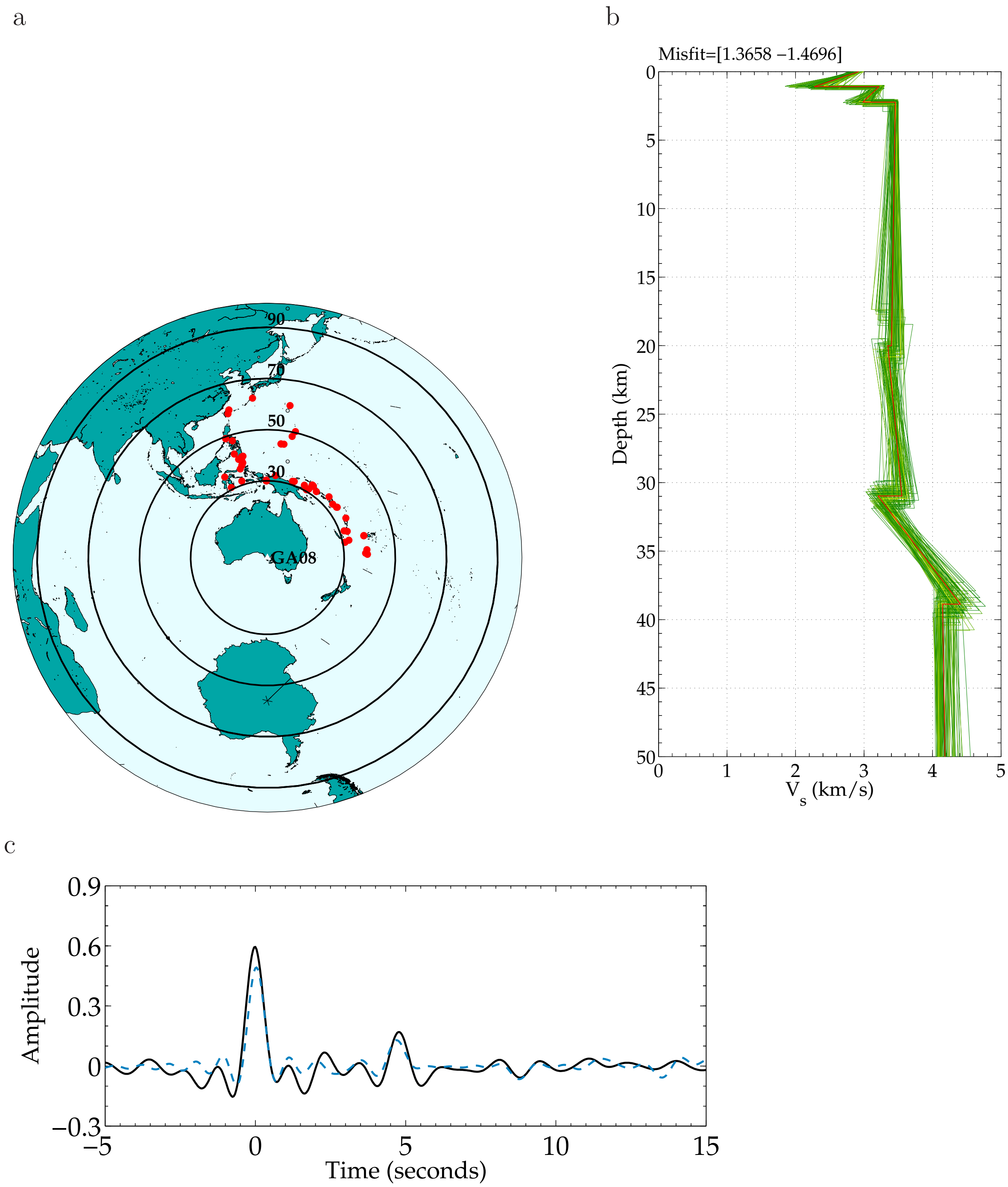

Figure 3.32: a) The distribution of the earthquakes for different distance ranges from GA08. b) Best 100 models and average model (red) from the combination of all inversions. c) The observed (black) and inverted (blue-dashed) radial receiver functions.

Station	Moho Depth (km)	Classification	Problem
TL01	X		Sediments - 27 km?
TL02	39	Intermediate	
TL03	41	Broad	
TL04	31	Intermediate	
TL05	37	Broad	
TL06	42	Sharp	
TL07	38	Sharp	
TL08	33	Broad	
TL09	X		Sediments - 40 km??
TL10	34	Intermediate	
TL11	X		Sediments - 35 km??
TL12	32	Sharp	
TL13	X		Poor Fit -30 km?
TL14	X		Poor Fit -30 km?
TL15	34	Sharp	
TL16	29	Intermediate	
TL17	X		Sediments - 3-D?
TL18	34	Broad	
TL19	X		Limited Fit-36 km?
TL20	X		Poor Fit
GA05	37	Intermediate	
GA06	X-40 km?		Poor Fit
GA07	33	Broad	
GA08	39	Broad	

Table 3.2: The estimated Moho depths for TL and GA stations. X stands for the poorly estimated depths due to the sedimentary zones and receiver function quality problems. Classification column comments on the nature of the Moho anomaly on the models. Problem column shows the associated problem with the particular station with poorly estimated Moho depths.

3.6 Crustal Depth Results

In this section, new crustal depth results from the receiver function analysis of TASMAL project stations are presented in the context of the geological setting of the stations. Crustal depth determinations from east Australia from the previous study by Clitheroe et al. (2000), with a sparser station distribution, are also included. The current study improves considerably on the coverage available to previous workers and delineates the geological transition between east and central Australia. The crustal thicknesses derived in this study, and by Clitheroe et al. (2000) for the region of the interest, are shown on top of the surface geology map of Australian continent at figure 3.33.

The crustal thickness varies significantly from central Australia to eastern Australia in the vicinity of the Tasman Line (shown with gray line). In the northern part of central Australia, the crustal thicknesses are 38, 42 and 41 km beneath the region corresponding to the east Arunta and north Mt. Isa Blocks. At the southeast edge of the Mt. Isa Block, crustal depths, including a result from Clitheroe et al. (2000), are shallower (at 35 and 31 km depth). Beneath the central part of the Thomson Orogen, crustal depths are rather shallow, and quite consistent (32, 32, 33, 35, 34 and 36 km) with deeper values being determined in the eastern Thomson Orogen (37, 39, 38 and 44 km). In stations located within the New England Orogen, crustal depth is fairly consistent (37, 36, 36 and 39 km).

The results from the Gawler Craton leg of the experiment show Moho depths of 39 and 40 km, with shallower values being obtained from stations covering the Adelaide Block (33, 37, 34, 36, and 34 km depth). There is a steady increase beginning from the Adelaide Block (Proterozoic Sediment) to the Gawler Craton. Clitheroe et al. (2000) noted that the Gawler Craton has a similar Moho nature with the Kimberley Craton in the north. Although geologically older than the Gawler Craton, Reading et al. (2003a) found similar Moho depths in average 40 km under Yilgarn Craton of Western Australia. In the Delamarian Orogen, a crustal depth value of 35 km was obtained while results from the Lachlan are generally deeper (38, 44 and 41 km) but are quite variable.

The new deployment has filled significant gaps in the knowledge of the crustal depth of the region of east Australia.

In receiver function analysis, it is often that the delayed peak and the

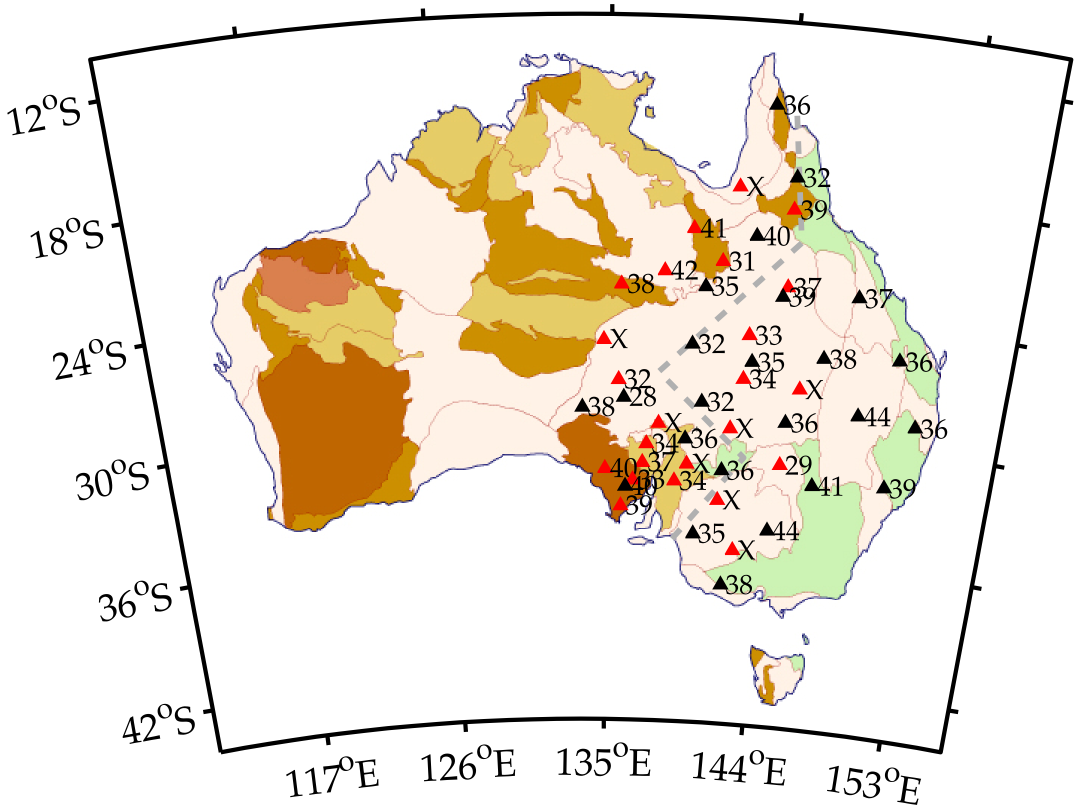

Figure 3.33: The crustal thicknesses derived from receiver function inversions. The red triangles show the results of this study and black triangles show the results from Clitheroe et al. (2000). Stations where a crustal thickness could not be determined are marked X. The gray dashed line is Tasman Line which marks the transition from the Precambrian west and central Australia to the Phanerozoic east.

ringing waveform indicate the presence of thick low velocity layers. The Moho signature is heavily masked in this situation therefore an inversion can not be pursued for constraining the crustal thickness. However, signals of this kind are good to characterize the vicinity of the stations with sedimentary features. In figure 3.33, these stations were marked with X. It should be noted that location of the stations also marks the transition between tectonic elements which matches the results of the receiver function study.

The Moho depths estimated from receiver functions exhibit a trend from the central Australia to eastern Australia, the images from group wavespeed tomography (given in Chapter 4) for the midcrust did not reveal a uniform transition for the same region.

3.7 Discussion

The results from the receiver function analysis of TASMAL experiment has a close agreement with the more sparsely distributed stations of Clitheroe et al. (2000).

The estimated crustal thicknesses indicate well the presence of the major tectonic blocks in the study area, e.g., Mt. Isa Block, Gawler Craton. In addition to this, stations located on thick sediments are revealed.

The stations located at the eastern part of the Tasman Line exhibits 3-D structure due to the differences in the receiver functions of different backazimuths. In contrast, the stations on the Thomson Orogeny exhibit consistent receiver functions for all backazimuths with similar and consistent crustal thicknesses.

The nature of the Moho transition shows differences correlated with the tectonic blocks. For example, transitional Moho is found beneath the stations of Mt. Isa Block with large crustal thicknesses. The refraction studies in this region found the Moho thickness around 55 km with a transition from a lower crust material to mantle material occurring in a 15 km thick zone (Goleby et al., 1998).

The consistent trend in crustal thicknesses from central Australia to the east may suggest the presence of Tasman Line. However, this trend diminishes in the northern and southern stations.

Although the methods used in this work are comparable to Clitheroe et al. (2000), note that the two studies differ on two points. Firstly, the employed inversion method; neighbourhood algorithm searches the parameter space more efficiently than the genetic algorithm, although both methods give good results when applied to receiver function analysis (Sambridge, 1999a). Secondly, the multitaper estimation gave stable estimates of receiver functions than the conventional spectral division with water-level correction employed in the work of Clitheroe et al. (2000)